

A New Stochastic Approach to Predict Peak and Residual Shear Strength of Natural Rock Discontinuities

D. Casagrande¹ · O. Buzzi¹ · A. Giacomini¹ · C. Lambert² · G. Fenton³

Received: 2 February 2017 / Accepted: 12 August 2017
© Springer-Verlag GmbH Austria 2017

Abstract Natural discontinuities are known to play a key role in the stability of rock masses. However, it is a non-trivial task to estimate the shear strength of large discontinuities. Because of the inherent complexity to access to the full surface of the large in situ discontinuities, researchers or engineers tend to work on small-scale specimens. As a consequence, the results are often plagued by the well-known scale effect. A new approach is here proposed to predict shear strength of discontinuities. This approach has the potential to avoid the scale effect. The rationale of the approach is as follows: a major parameter that governs the shear strength of a discontinuity within a rock mass is roughness, which can be accounted for by surveying the discontinuity surface. However, this is typically not possible for discontinuities contained within the rock mass where only traces are visible. For natural surfaces, it can be assumed that traces are, to some extent, representative of the surface. It is here proposed to use the

available 2D information (from a visible trace, referred to as a seed trace) and a random field model to create a large number of synthetic surfaces (3D data sets). The shear strength of each synthetic surface can then be estimated using a semi-analytical model. By using a large number of synthetic surfaces and a Monte Carlo strategy, a meaningful shear strength distribution can be obtained. This paper presents the validation of the semi-analytical mechanistic model required to support the new approach for prediction of discontinuity shear strength. The model can predict both peak and residual shear strength. The second part of the paper lays the foundation of a random field model to support the creation of synthetic surfaces having statistical properties in line with those of the data of the seed trace. The paper concludes that it is possible to obtain a reasonable estimate of peak and residual shear strength of the discontinuities tested from the information from a single trace, without having access to the whole surface.

✉ O. Buzzi
Olivier.Buzzi@newcastle.edu.au

D. Casagrande
Davide.Casagrande@uon.edu.au

A. Giacomini
Anna.Giacomini@newcastle.edu.au

C. Lambert
clambert@golder.co.nz

G. Fenton
gordon.fenton@dal.ca

¹ Priority Research Centre for Geotechnical Science and Engineering, University of Newcastle, Callaghan, NSW 2208, Australia

² Golder Associates, Christchurch, New Zealand

³ Dalhousie University, Halifax, NS, Canada

Keywords Rock joint · Discontinuity · Shear strength · Random field · Stochastic · Scale effect

List of symbols

x, y, z	Coordinates of points on the discontinuity surface
Δx	Spatial increment in direction x
c	Material cohesion (obtained from triaxial tests)
ϕ	Material friction angle (obtained from triaxial tests)
ϕ_b	Basic friction angle
m_i	Hoek–Brown strength parameter
σ_{ci}	Hoek–Brown strength parameter
σ_1	Major principal stress
σ_3	Minor principal stress

β_{app_i}	Apparent dip of facet i
\bar{n}_i	Unit vector normal to facet i
\bar{s}	Unit vector indicating the shear direction
β^*	Variable used to identify active facets
N_{cf}	Total number of contributing facets at a given value of β^*
A_i	Facet area
A_{ip}	Facet area projected on the xy plane
A_{tot}	Total discontinuity area
σ_{local_i}	Local vertical normal stress acting on facet i
$f_{sliding_i}$	Local horizontal force required to slide on facet i
f_{shear_i}	Local horizontal force required to shear facet i
F_{macro}	Vertical force exerted on the whole discontinuity
f_{local_i}	Local vertical force exerted on facet i
f_{peak}	Peak shear force predicted by the model
$f_{residual}$	Residual shear force predicted by the model
τ	Shear stress
τ_p	Peak shear strength
τ_{res}	Residual shear strength
$\tau_{p-predicted}$	Peak shear strength predicted by the model
τ_{p-exp}	Experimentally measured peak shear strength
$\tau_{res-predicted}$	Residual shear strength predicted by the model
$\tau_{res-exp}$	Experimentally measured residual shear strength
$\langle \tau_p \rangle$	Mean peak shear strength
$\langle \tau_{res} \rangle$	Mean residual shear strength
ρ	Correlation coefficient
θ	Correlation length
d	Distance between two discrete data
σ_i	Standard deviation of gradients
σ_z	Standard deviation of heights
σ_z^2	Variance of heights
i_x	Gradient in direction x
i_y	Gradient in direction y
JRC	Joint roughness coefficient
ΔZ	Difference in surface heights between successive measurements
z_{model}	Surface height predicted by the model
z_{exp}	Experimental value of surface height
δ_n	Normal displacement
δ_s	Tangential displacement
σ_{no}	Initial normal stress applied to the specimen during shear test at constant normal force
σ_n	Normal stress applied to the specimen during shear test at constant normal stress or normal stress applied to the specimen at peak shear strength (for tests under constant normal force)

1 Introduction

It has been long recognised that the hydro-mechanical behaviour of a rock mass is strongly influenced by the presence of discontinuities (Goodman 1989; Brady and Brown 1985). Figure 1 is a clear illustration of the problem. The photograph represents a fractured rock mass along the coastal fringe in the vicinity of Newcastle, Australia, where fallen blocks are clearly visible. These blocks have detached along horizontal and sub-vertical discontinuities, which constitute weaknesses within the rock mass. Assessing the stability of such blocks, and to some extent, that of the rock mass, necessitates an estimate of the shear strength of the discontinuities.

The shear strength of rock joints has been the subject of significant attention for several decades. Researchers have investigated key factors such as the mechanical response (Barton 1976; Bandis et al. 1983; Barton et al. 1985; Zhao 1996; Johnston and Kodikara 1994); the scale effect (Barton and Bandis 1980; Fardin et al. 2001, 2004; Vallier et al. 2010); the hydro-mechanical couplings (Witherspoon et al. 1980; Gale 1982; Raven and Gale 1985; Brown 1987; Esaki et al. 1999; Indraratna and Ranjith 2001; Lee and Cho 2002; Koyama et al. 2006; Giacomini et al. 2008); the phenomenon of asperity degradation (Hutson and Dowing 1990; Boulon et al. 1993); and the effects of filling and boundary conditions (Ladanyi and Archambault 1977; Indraratna et al. 1998, 2014; de Toledo and de Freitas 1993). Of all the factors controlling the behaviour of rock discontinuities, roughness is one of the most critical. Extensive effort has been spent characterising surface roughness via classical tribology, geostatistical approaches (Ferrero and Giani 1990; Tse and Cruden 1979; Marache



Fig. 1 Photograph of a fractured rock mass in Newcastle, NSW, Australia (photograph by O. Buzzi)

et al. 2002), fractal theory (Seidel and Haberfield 1995; Carr and Warriner 1989) and empirical methods (Barton and Choubey 1977). To date, there is no consensus on the most appropriate way to characterise joint roughness, although the joint roughness coefficient (JRC) defined by Barton and Choubey (1977) appears to be the most used roughness descriptor.

In parallel to experimental investigations, significant progress has been made on the modelling front. From the pioneering works of Patton (1966) and Barton (1976), a number of constitutive laws or mechanistic models have been proposed to predict the behaviour of rock joints (e.g. Plesha 1987; Haberfield and Johnston 1994; Seidel and Haberfield 2002; Vallier et al. 2010; Zandarin et al. 2013). Recently, a number of newer sophisticated empirical models have been proposed in the literature (e.g. Grasselli and Egger 2003; Yang et al. 2016).

The substantial progress in computational power that has occurred in the past decades has seen a number of models of rock joints being implemented in finite elements (Selvadurai and Yu 2005; Gens et al. 1990), discrete elements (Cundall 2000; Bahaaddini et al. 2013; Lambert et al. 2010) or hybrid finite–discrete elements (Karami and Stead 2008; Grasselli et al. 2014). Although current numerical models do offer a number of advantages, they also suffer from inherent limitations: capturing asperity degradation remains a challenge, computational times are still high and, most importantly, an accurate numerical simulation is only possible if the surface morphology is available. This encourages the modelling of relatively small specimens, as large joint surfaces are typical not available in situ (unless a block has already fallen, which defeats the purpose of shear strength prediction).

With numerical models and laboratory tests mainly pertaining to small rock specimens, shear strength results are not directly transferable to a large scale, because of the well-known “scale effect” (Barton and Bandis 1980). To date, although knowledge on rock joints has advanced significantly on multiple fronts, the scale effect remains a challenge to understand or predict. Despite many attempts to address the scale effect, either via fractal approaches (Vallier et al. 2010; Li et al. 2016; Giacomini et al. 2008) or experimental correlations (Bandis et al. 1981), as far as the authors know, there is still no consensual or practical method available in the literature. Working directly at the relevant scale for engineering purposes is not trivial, and there is currently no satisfactory method to estimate the shear strength of a large in situ discontinuity. Researchers and engineers often resort to the joint roughness coefficient (JRC) defined by Barton and Choubey (1977) and its associated empirical shear behaviour model. However, this is largely due to convenience and a lack of a reliable alternative. Barton himself recognises that there has been some confusion about his model (Barton 2013). Furthermore, the JRC is known to be

scale dependent (it is defined on a 10 cm length) and its value depends on the method chosen to ascertain it, i.e. Barton’s comb, statistical correlation (e.g. via Z_2) or tilt test.

The research presented in this paper proposes an alternative to the traditional deterministic approach and tackles the issue of shear strength from a stochastic perspective and using a random field model, with the possibility to apply it at a large (field) scale. Stochastic analysis per se is not new in rock mechanics: it is a strategy that has been used to create discrete fracture networks (e.g. Lambert et al. 2012; Xu and Dowd 2014; Noorian-Bidgoli and Jing 2015), to reproduce some types of rough joint surfaces (Lanaro 2000) and to distribute flaws within a rock matrix (Krumbholz et al. 2014). However, as far as the authors are aware, there has been no attempt, to date, to predict shear strength of discontinuities from a stochastic perspective.

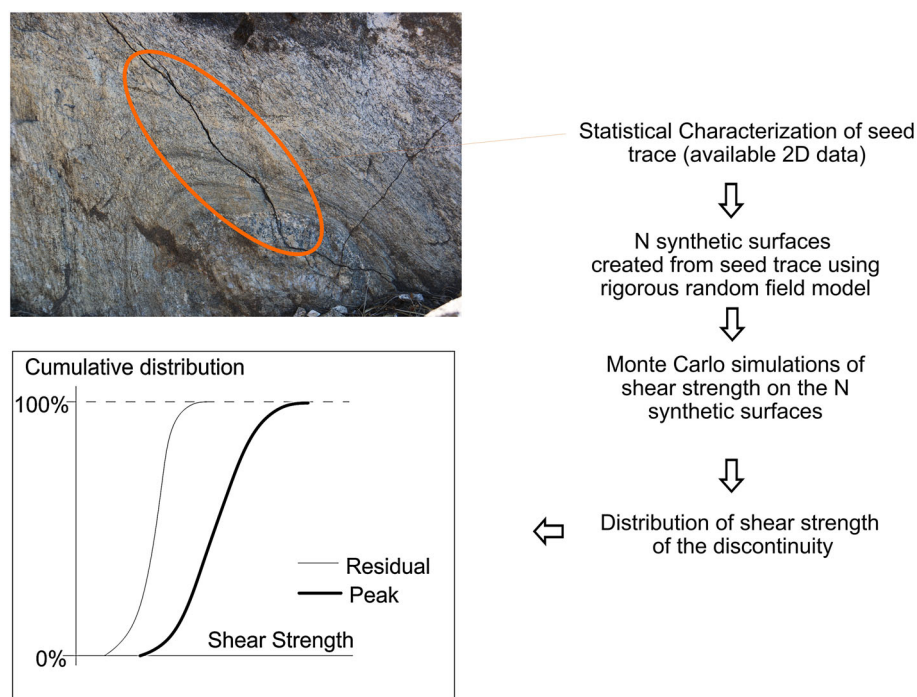
This paper includes two parts. The description and validation of a new semi-analytical model that can predict peak and residual shear strength of a discontinuity is first presented. Unlike most existing models, this mechanistic model is simple to implement and runs in a matter of seconds, which implies that a large number of simulations, compatible with Monte Carlo techniques, are possible in a reasonable time. Although the model is inspired by the work of Huang et al. (2002), there are a number of novel and important aspects in the work presented herein: the model handles real 3D surfaces, as opposed to 2D idealised ones (e.g. saw-tooth), the facets are smaller than the asperities, which has implications on the way the whole asperity shearing is modelled, and the model predicts both peak and residual shear strength.

The second part of the paper lays the foundation for the new stochastic approach for rock joints. It presents the application of a random field model to the prediction of shear strength. As it is of utmost importance to first establish a rigorous framework, the research first pertains to laboratory-scale specimens under controlled conditions, not large-scale discontinuities. Working under controlled conditions allows defining the influence of key parameters of the random field model and identify which roughness descriptor is the most suited to this new approach. At this stage, prediction of shear strength of full-scale discontinuities, with their inherent complexities such as filling, weathering, persistence, opening and pore pressure, has not yet been attempted. Yet, it is believed that this approach can be applied to large in situ discontinuities.

2 Rationale of the New Approach for Discontinuity Shear Strength Prediction

Roughness is one of the key parameters that govern the shear strength of a discontinuity and that is usually captured by accurately surveying a discontinuity surface. However, such survey is not possible for surfaces

Fig. 2 Key steps of the new stochastic approach to predicting shear strength of natural discontinuities



contained within a rock mass and for which only traces are visible. For natural surfaces, it can be assumed that traces are, to some extent, representative of the non-accessible surface. The idea of the new approach is to use the available information directly at the discontinuity scale, from the visible traces (here called seed traces), to support the creation of a large number of synthetic surfaces (3D) via a random field model (Vanmarcke 1983; Fenton 1990; Fenton and Griffiths 2008). The random field model relies on the statistics of the input data set (i.e. seed trace) to produce a random data field of similar statistical characteristics, namely the synthetic surfaces that are possible representations of the real discontinuity surface.

In a next step, a distribution of strength is obtained by predicting the shear strength of all these synthetic surfaces. Note that the prediction could be achieved via any shear strength model but, because a large number of surfaces should be tested to reach a statistically sound result, it is important to use a time-efficient model. Here, a semi-analytical model has been developed to support the validation of the new stochastic approach for shear strength prediction. Figure 2 summarises the key points of the new approach.

3 Description of the Semi-Analytical Model for Shear Strength

This section details the key aspects of the model. Explanations are supported by a flow chart (Fig. 3) and schematics (Figs. 4, 5, 6).

3.1 General Principle

The key idea of the model is to add the contribution of all asperities that are mobilised during shearing (referred to as “active” or “contributing” asperities). The concept of active asperities derives from the fact that when a joint dilates during shearing, dilation occurs along the steepest asperities, leading to a slight opening of the interface and a redistribution of the load. These active asperities are then sheared off, and the load is redistributed onto other asperities that will then be sheared off. This process is repeated until no more shearing occurs. The rest of the section will show that such progressive shearing process is captured by the model and is reflected in a progressive modification of the surface geometry.

3.2 Model Inputs

The surface data, organised in a gridded xyz matrix (i.e. with a constant and equal step long x and y directions), constitute one of the inputs of the model. The joint is assumed to be perfectly matching. Shearing occurs along the xy plane, and z represents the distance from the xy plane. Note that, by convention, the lowest point of the surface is allocated a value of $z = 0$ mm. Other model inputs are the shearing direction (within the xy plane), the value of normal stress and the material strength parameters (c and ϕ for Mohr–Coulomb or m_i and σ_{ci} for Hoek–Brown). Note that the model relies on a Mohr–Coulomb criterion to predict local shearing of asperities. If Hoek–

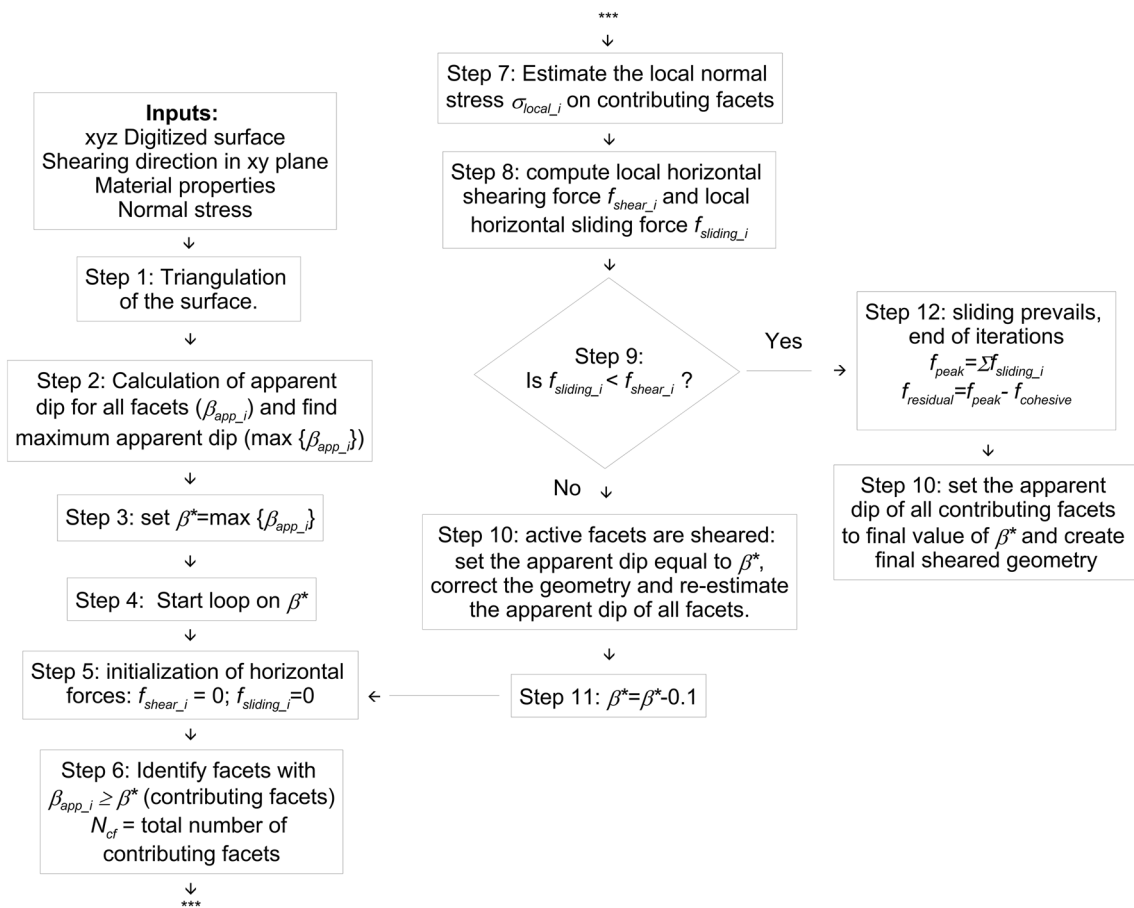


Fig. 3 Flow chart representing the key steps of the analytical model for shear strength

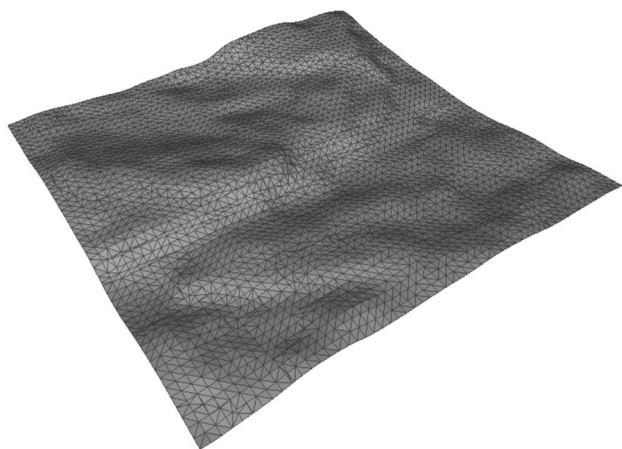


Fig. 4 Example of triangulated surface. Surface dimensions are approximately 10 cm per 10 cm. The surface contains one data point every 1.5 mm in both directions

Brown parameters are entered, equivalent friction angle and cohesion will be defined as:

$$\sin \phi = \frac{K - 1}{K + 1} \tag{1}$$

and

$$c = \frac{\sigma_{ci} \cdot (1 - \sin \phi)}{2 \cdot \cos \phi} \tag{2}$$

where $K = d\sigma_1/d\sigma_3$ with σ_1 the major principal stress and σ_3 the minor principal stress.

All the inputs are reported at the beginning of the flow chart (Fig. 3).

3.3 Identifying the Active Facets

The first step of the model (step 1 in Fig. 3) consists of triangulating the surface to create facets, as illustrated in Fig. 4. Note that the surface in Fig. 4 only has a data point every 1.5 mm (in each direction) so that the facets are clearly visible. The surfaces used for the model actually have one data point every 0.5 mm in each direction. The concept of apparent dip, defined by Grasselli (2006), is used to indicate how steep the facets are with respect to the shearing direction and, hence, whether they are active or not. The apparent dip of facet i (β_{app_i}) is calculated as:

$$\beta_{app_i} = a \cos(\bar{n}_i \cdot \bar{s}) - 90 \tag{3}$$

Fig. 5 **a** Representation of a dilating interface with two active facets remaining in contact. The vertical force applied to the discontinuity F_{macro} is balanced by two equal forces f_{local_i} , applied at the two facets in contact. **b** 2D representation of the interface and two active facets being either sheared at their base or slid upon. The facet area is noted A_i , and the area projected on the xy plane is noted A_{ip}

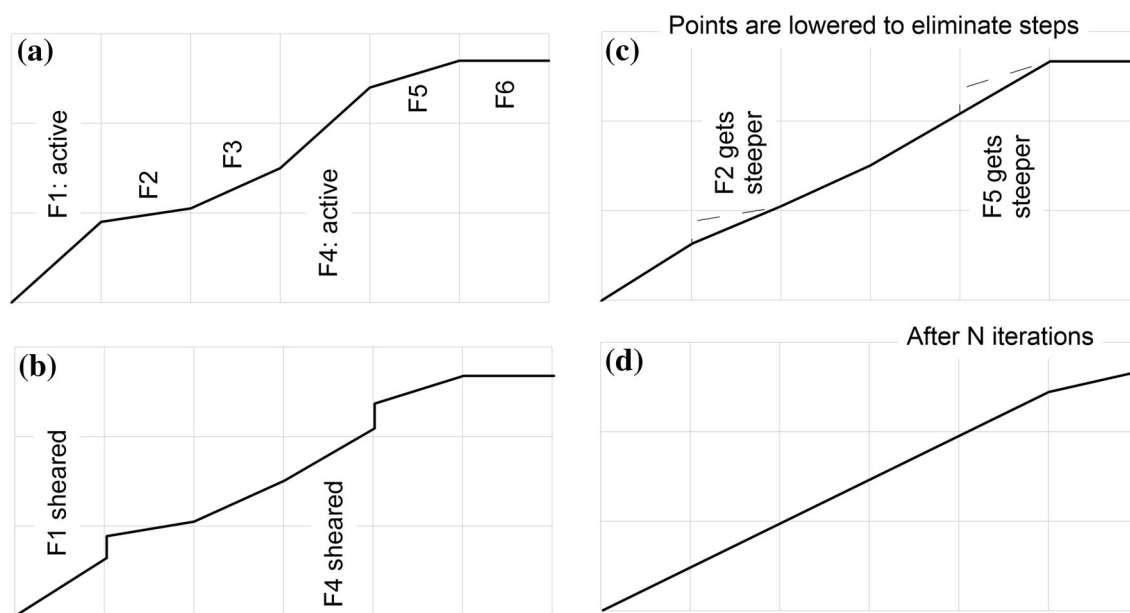
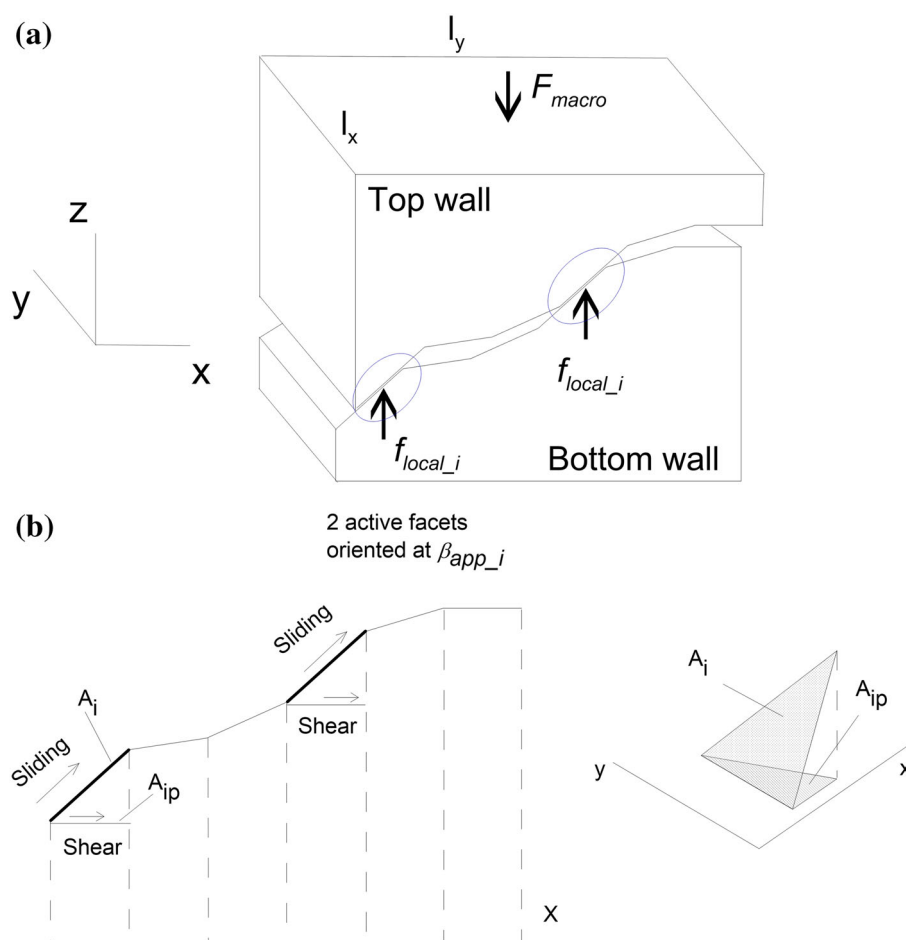


Fig. 6 **a** Initial 2D profile of the interface showing six facets (F1–F6). **b** Sheared profile showing steps resulting from local shearing. **c** Corrected profile with steepening of facets 2 and 5. **d** Profile after N iterations and progressive shearing. Facets 1–5 have been

progressively sheared, and their apparent dip has been reduced. As a result of the step correction, facet 6 has steepened. At this stage, sliding predominates and iterations stop

where \bar{n}_i is the unit vector normal to facet i and \bar{s} is the unit vector indicating the shear direction in the discontinuity plane (i.e. xy plane). $(\bar{n}_i \cdot \bar{s})$ is the dot product of both vectors. In the following, the shearing direction in the xy plane will be referred to as “horizontal”.

Step 3–step 11 of Fig. 3 define the loop where the model progressively identifies all active facets, from the steepest and decreasing in steepness, and computes their contribution to shear resistance. The loop uses the test variable β^* which progressively decreases from the maximum apparent dip of all facets, towards zero in 0.1 decrements. At each decrement (i.e. each value of β^*), all facets having an apparent dip (β_{app_i}) larger than or equal to β^* are considered active and can possibly be sheared. The loop on β^* stops when no more shearing occurs (this will be detailed in the next section).

3.4 Computing Shearing and Sliding Forces

The model assumes that all active facets, regardless of their apparent dip, are in contact. The justification of this assumption will be given. As a result, the vertical force exerted on the whole discontinuity (F_{macro}) is uniformly distributed amongst all active facets that are subjected to a local vertical force f_{local_i} equal to:

$$f_{local_i} = \frac{F_{macro}}{N_{cf}} \tag{4}$$

where N_{cf} is the total number of contributing facets at a given decrement of β^* (see Fig. 5a).

The local vertical normal stress is then estimated for each contributing facet as:

$$\sigma_{local_i} = \frac{f_{local_i}}{A_{ip}} \tag{5}$$

where A_{ip} is the area of the facet projected on the xy plane (see Fig. 5b). Note that, although a relative tangential displacement is shown in Fig. 5a in order to explain why only the active facets are in contact, the model does not account for any displacement. As a consequence, it is considered that contact occurs over whole active facets, not only partially as depicted in Fig. 5a.

Equation (5) is associated with step 7 in the algorithm of Fig. 3. As shown in Fig. 5a, there can be several active facets and hence several points of contact, at any decrement of β^* .

Estimating the contribution of each active facet to shear resistance begins with computing the local horizontal force required to slide on the facet ($f_{sliding_i}$, acting on A_i) and the local horizontal force required to shear the facet along a horizontal plane (f_{shear_i} acting on A_{ip}). Indeed, two scenarios are here considered: a facet of the top wall can slide on its bottom counter part, along surface A_i , or the bottom facet can be sheared. In this case, it is assumed that shearing occurs

along the base of the facet, along a horizontal plane, as this minimises the shear resistance (over surface A_{ip} , see Fig. 5b). $f_{sliding_i}$, and f_{shear_i} are given by Eqs. (6) and (7):

$$f_{sliding_i} = f_{local_i} \cdot \tan(\phi_b + \beta_{app_i}) \tag{6}$$

$$f_{shear_i} = A_{ip} \cdot (c + \sigma_{local_i} \cdot \tan(\phi)) \tag{7}$$

where β_{app_i} is the facet apparent dip, ϕ is the Mohr–Coulomb friction angle of the material, c is the cohesion, ϕ_b is the basic friction angle, A_{ip} is the area of the facet projected on the xy plane (see Fig. 5b) and σ_{local_i} is the local vertical stress (along z axis) acting on facet i [see Eq. (5)].

Local shearing of the facet will only occur if the shear resistance is lower than the sliding resistance, i.e. $f_{shear_i} \leq f_{sliding_i}$ (see step 9 of the flow chart in Fig. 3).

Shearing tends to prevail over sliding at the beginning of the iterations, when the facets are steep enough. As progressive shearing takes place, the asperities flatten (process to be detailed in the next section) until a point where sliding prevails over shearing and the iterations stop.

3.5 Progressive Modification of Asperity Geometry

The surface geometry is only modified if shearing of facets takes place. Although the shear resistance is calculated along the horizontal plane corresponding to the base of the facet [Eq. (7)], physical shearing of the facet is imposed along a plane oriented at β^* . It is an assumption of the model, which allows the progressive shearing of facets and avoids unrealistically flat surfaces at the end of the process. Each time a facet is sheared, a step is created at the junction with adjacent facet (see Fig. 6a, b). Such steps are not commonly observed after shearing, so the strategy employed here is to correct the geometry as per Fig. 6c. Adjusting points of the surface can locally increase the apparent dip of some facets (e.g. facets 2 and 5 in Fig. 6c) that can become active and be sheared. After a number of iterations, the apparent dip has reduced enough that sliding becomes predominant over shearing of the facets (Fig. 6d) and the iterations stop.

3.6 Model Outputs

The model predicts the peak shear strength and the sheared surface geometry, from which it can estimate the residual shear strength. As stated in Sect. 3.4, the iterations on β^* stop when it takes less force to slide over the active facets than to shear them (step 9 in flow chart in Fig. 3). At that stage, the contribution of all active facets is only frictional and is calculated by Eq. (6). The peak shear force f_{peak} is the sum of the contribution of all active facets (step 12):

$$f_{peak} = \sum_{i=1}^{N_{cf}} f_{sliding_i} = \sum_{i=1}^{N_{cf}} f_{local_i} \cdot \tan(\phi_b + \beta_{app_i}) \tag{8}$$

where f_{sliding_i} is the local horizontal force required to slide over active facet i and N_{cf} is the total number of active facets for a given value of β^* . The peak shear strength $\tau_{p\text{-predicted}}$ is simply the peak shear force over the total discontinuity area (A_{tot} equal to l_x per l_y , see Fig. 5a):

$$\tau_{p\text{-predicted}} = f_{\text{peak}}/A_{\text{tot}} \quad (9)$$

“Appendix A” provides an example of calculation of shear strength for the last two decrements pertaining to the surface shown in Fig. 6a.

The residual shear strength is calculated from the peak shear force by considering that the difference between peak and residual forces is the cohesive contribution of all sheared asperities:

$$f_{\text{residual}} = f_{\text{peak}} - c \cdot N_{\text{cf}} \cdot A_{\text{ip}} \quad (10)$$

where f_{peak} is estimated as per Eq. (8), c is the material cohesion, N_{cf} is the total number of active facets and A_{ip} is the facet area projected on the xy plane (see Fig. 5b). The residual shear strength is then expressed as:

$$\tau_{\text{res-predicted}} = \frac{f_{\text{residual}}}{A_{\text{tot}}} \quad (11)$$

As the value of β^* is progressively reduced, the sliding force reduces (it gets easier to slide on facets) and the shearing force increases (more facets are being sheared) until both forces converge, as illustrated in Fig. 7.

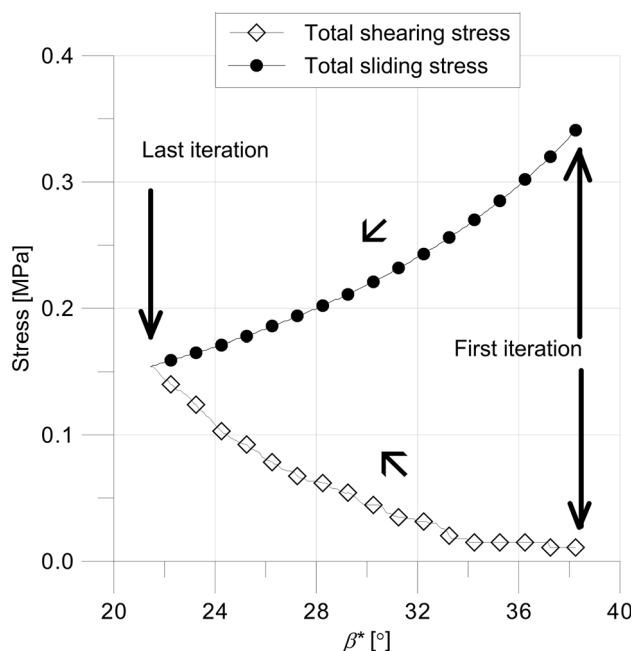


Fig. 7 Evolution of the total shearing stress (defined as $(\sum_{i=1}^{N_{\text{cf}}} f_{\text{sliding}_i}/A_{\text{tot}})$) and total sliding stress (defined as $(\sum_{i=1}^{N_{\text{cf}}} f_{\text{shear}_i}/A_{\text{tot}})$) as β^* reduces from maximum value to final value (note that one marker is plotted every ten values). Surface sheared under a normal stress of 0.1 MPa

4 Description of the Random Field Model for Natural Discontinuities

A random field model is a probabilistic model that permits the generation of random data set from an initial data set. Such model does more than simply producing data following a given distribution; it allows some degree of correlation between the data points, usually as a function of the distance separating the points (Fenton and Griffiths 2008). In other words, the data points modelled are not independent from one another. The spatial correlation is achieved via the so-called correlation length. The local average subdivision (LAS) algorithm developed by Fenton and Vanmarcke (1990) was here used to generate random but correlated data.

It is possible to create a random surface by generating a random field of asperity heights (most intuitive parameter to describe a surface) or a field of gradients (parameter controlling the shear strength in the analytical model). Decision as to which variable is to be modelled should be made after due consideration of the two following points:

1. It will be shown in a later section that, for the surfaces tested in this research, the asperity heights distribution does not follow any known distribution and cannot be mathematically defined. In contrast, the distribution of gradients was found to be approximately normal for most traces. Considering that the distribution of input data has to be mathematically defined in order to apply the random field model, it seems more appropriate to create a random field of gradients rather than a random field of asperities.
2. Creating a random surface from gradients poses some issues. Although integrating the gradients of a trace along direction x yields the relative height of all points of the trace, an initial height has to be arbitrarily selected. This process can be repeated for all parallel traces of the surface, i.e. all traces in direction x , in order to generate the height field. However, for each trace, a decision has to be made on the initial height and there is no guarantee that the resulting gradient distribution in the perpendicular direction (y) would be realistic, since all the traces have been reconstructed independently from one another.

In short, modelling gradients seems more correct but reconstructing a surface from gradients is difficult. Bearing in mind that the objective of the random field model is to create a field having a Gaussian distribution of gradients, the following solution was adopted here: a random field of heights was created with the assumption that the data follow a normal distribution (with mean and standard deviation corresponding to those of the data set). As a

Table 1 Relevant properties of the mortar used to create the replicas

Unconfined compressive strength (MPa)	Basic friction angle (°)	Apparent cohesion (MPa)	Friction angle (°)	m_i (from Hoek–Brown criterion)
Mean: 39.67	Mean: 35.30	4.74	58.1	35.2
SD: 5.47	SD: 0.19			

SD standard deviation

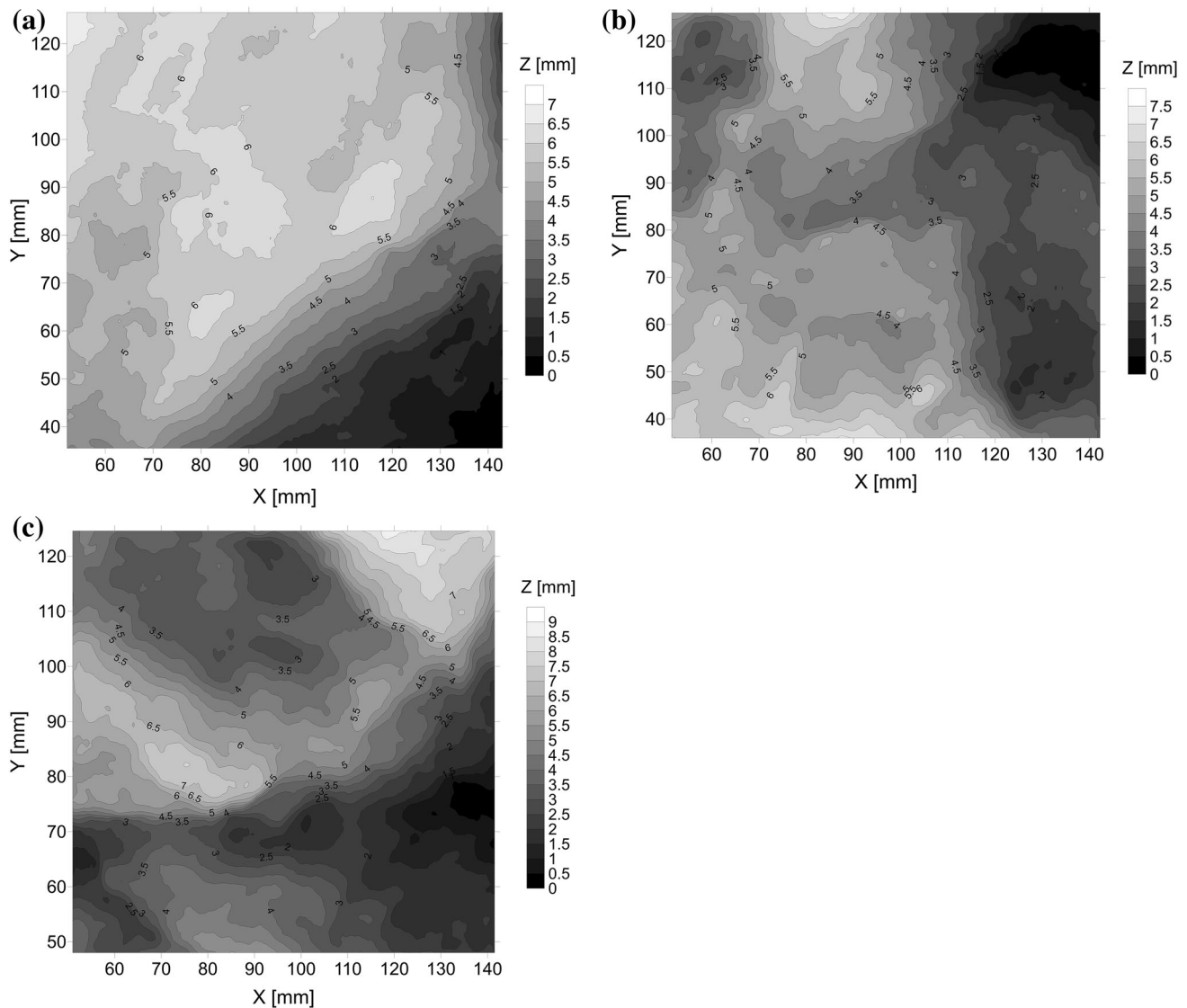


Fig. 8 Representation of the three surfaces (S, M, R) used to validate the semi-analytical model for shear strength and the new stochastic approach for the prediction of shear strength. **a** Surface S, **b** surface M, **c** surface R

consequence, the derivative of the field created (i.e. gradients) does also follow a normal distribution. The points mentioned above are then reconciled.

The random field model requires the definition of a correlation coefficient (ρ), which is a function of the correlation length (θ) and the distance between two points (d). A Gaussian correlation formulation, which is common in

geotechnical engineering (Fenton and Griffiths 2008), has been used here:

$$\rho(d) = e^{-\pi \cdot \left(\frac{d}{\theta}\right)^2} \tag{12}$$

Equation (12) describes how the degree of correlation between two points, quantified by ρ , decreases as the distance between the points (d) increases. The rate at which

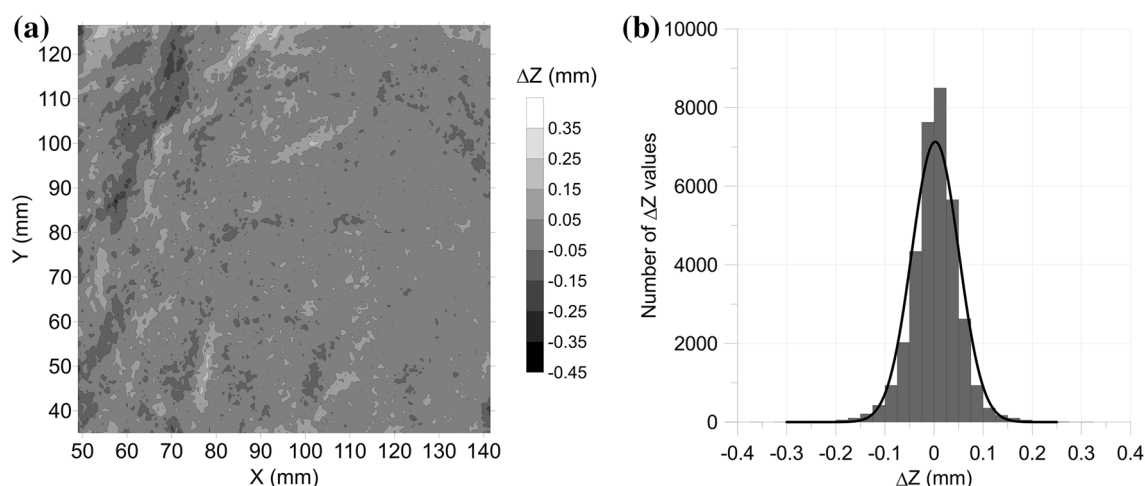


Fig. 9 Differences in height between two successive measurements of surface M by photogrammetry. **a** Map of the differences, **b** histogram of differences

the correlation coefficient ρ decreases is governed by the correlation length θ , defined as:

$$\theta = \Delta x \cdot \sqrt{\frac{-\pi}{\ln\left(1 - \frac{1}{2}\left(\frac{\Delta x \cdot \sigma_i}{\sigma_z}\right)^2\right)}} \quad (13)$$

where σ_i is the standard deviation of gradients (gradients are defined in “Appendix B”), σ_z is the standard deviation of heights and Δx is spatial increment in direction x . The reader can refer to “Appendix B” for the full derivation of θ .

Note that a correlation length can be estimated for any data set, i.e. for the whole surface or for each trace. Finally, an assumption of roughness isotropy was made, which implies that the value of correlation length estimated via Eq. (13) is considered to be isotropic. It is beyond the scope of the present paper to implement roughness anisotropy in the random field model.

5 Experimental Facilities and Experimental Programme

5.1 Materials and Discontinuities

Three natural discontinuities, of different roughness, coming from sedimentary rocks of the Hunter Valley (NSW, Australia) were selected for this study. Measurements with Barton’s comb returned JRC values of 2–4, 8–10 and 16–18 for the three surfaces. In the following, the smooth, medium and rough surfaces will be referred to as S, M and R, respectively. Moulds of each natural surface were created using Silastic polymer in order to produce replicas and conduct multiple tests on the same

morphology. The replicas were made of a mortar containing 14% of water, 30% of cement and 56% of the fraction passing the 0.6-mm sieve of medium-grained silica sand from Stockton Beach, NSW, Australia. The two walls of the discontinuities were created by casting some mortar (referred to as part A) against the original surface and then casting some mortar against part A in order to obtain a perfectly matching part B. All shear tests were conducted after a week of curing in a fog room, time after which mortar specimens were tested under unconfined compression and triaxial compression (as per 1978 ISRM recommended method, length-to-diameter ratio of 2.5) and for basic friction angle (following ISRM recommended method). Relevant material properties are provided in Table 1.

5.2 Photogrammetry

Applying and validating the new analytical model requires capturing the morphology of each surface, pre- and post-shearing, which was achieved via photogrammetry. The specimens were placed on a rotating table with a camera (Canon 7D EOS equipped with a 50-mm lens) located about 1 m away from the specimen. A total of 80 rotations were imparted to the specimen, and each time, a photograph was taken. The Agisoft Photoscan software was used to process the data and create a gridded data file. Figure 8 shows the contour map of the surfaces considered here and the corresponding replicas.

The accuracy of measurement was estimated to 25 μm , and a repeatability exercise, conducted on surface M, shows a normally distributed error with a standard deviation of about 0.08 mm and an average around 0 mm (Fig. 9).

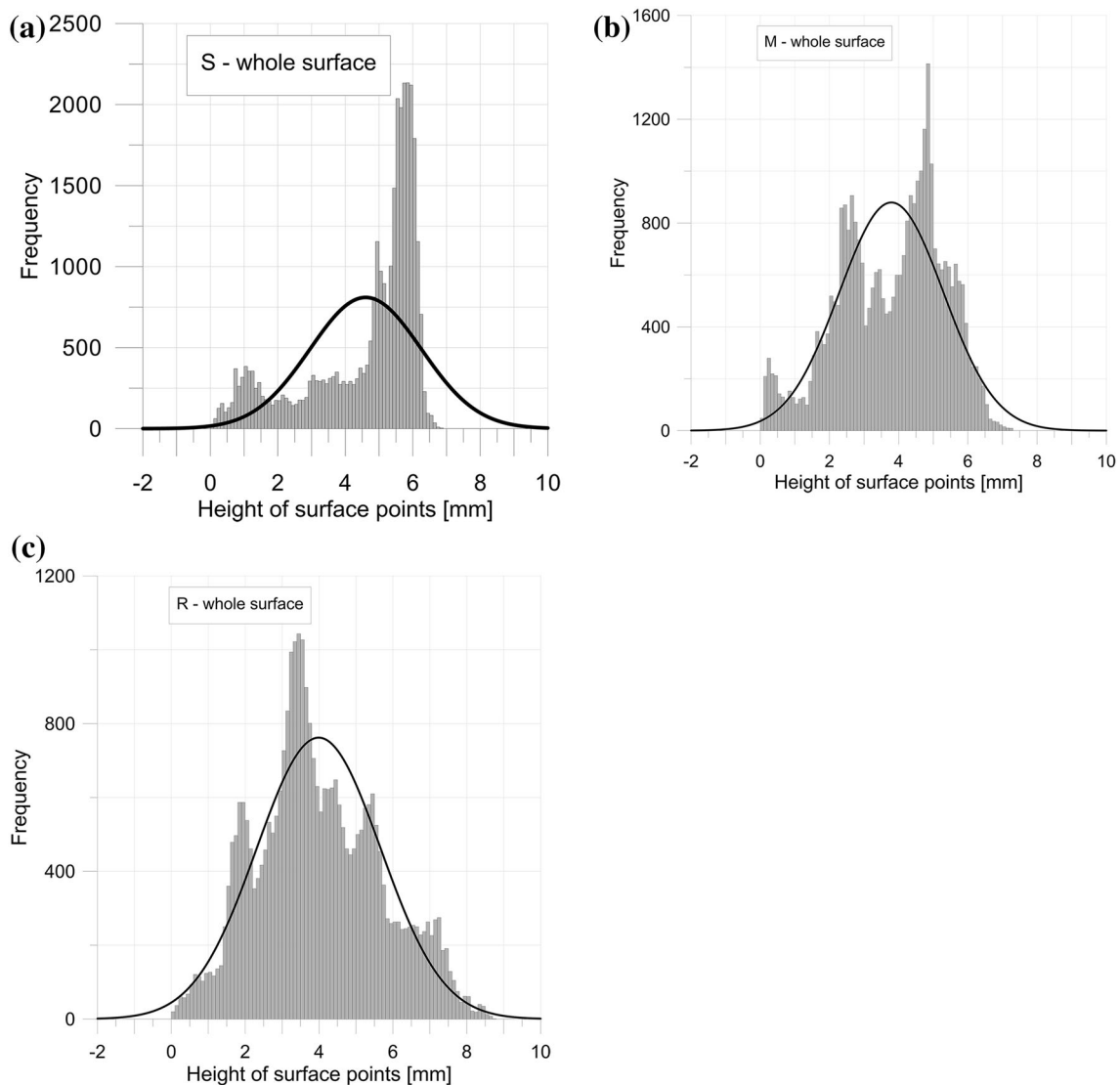


Fig. 10 Histograms of heights of the points constituting surfaces S (a), M (b) and R (c). The continuous line corresponds to a Gaussian distribution calculated from the mean and standard deviation of the data set

5.3 Statistical Analysis of Surfaces

A statistical analysis of the three surfaces was conducted in order to identify the adequate descriptors of surface morphology that will underpin the rigorous transfer of 2D data set (seed trace) towards a 3D random field (synthetic surface) via the random field model. The most intuitive parameter to describe the surface morphology is the height (noted z , in mm) of every point of the surface. However, Fig. 10 shows that the histogram of height values does not follow any specific distribution, making it difficult to mathematically define the initial data set and, hence, the target statistical properties of the synthetic surfaces.

In contrast, visual inspection of the histograms gradients along the x axis (axis defined in Fig. 8) suggests that the

distribution of gradients (defined by Eqs. (14) and (15) of “Appendix B”) is close to Gaussian (Fig. 11). For the sake of conciseness, results pertaining to gradients along y axis are not shown but their distribution was also found to be Gaussian.

It is here relevant to consider that each trace has its own mean and standard deviation of gradients and heights. These parameters differ from trace to trace, as demonstrated by Fig. 12.

The variability of sample mean and sample standard deviation of gradient values from trace to trace (as depicted in Fig. 12) will translate into a variability in sample correlation length, calculated according to Eq. (13), as shown in Fig. 13.

Figure 13 raises the question of the influence of the properties of the seed trace on the estimate of shear

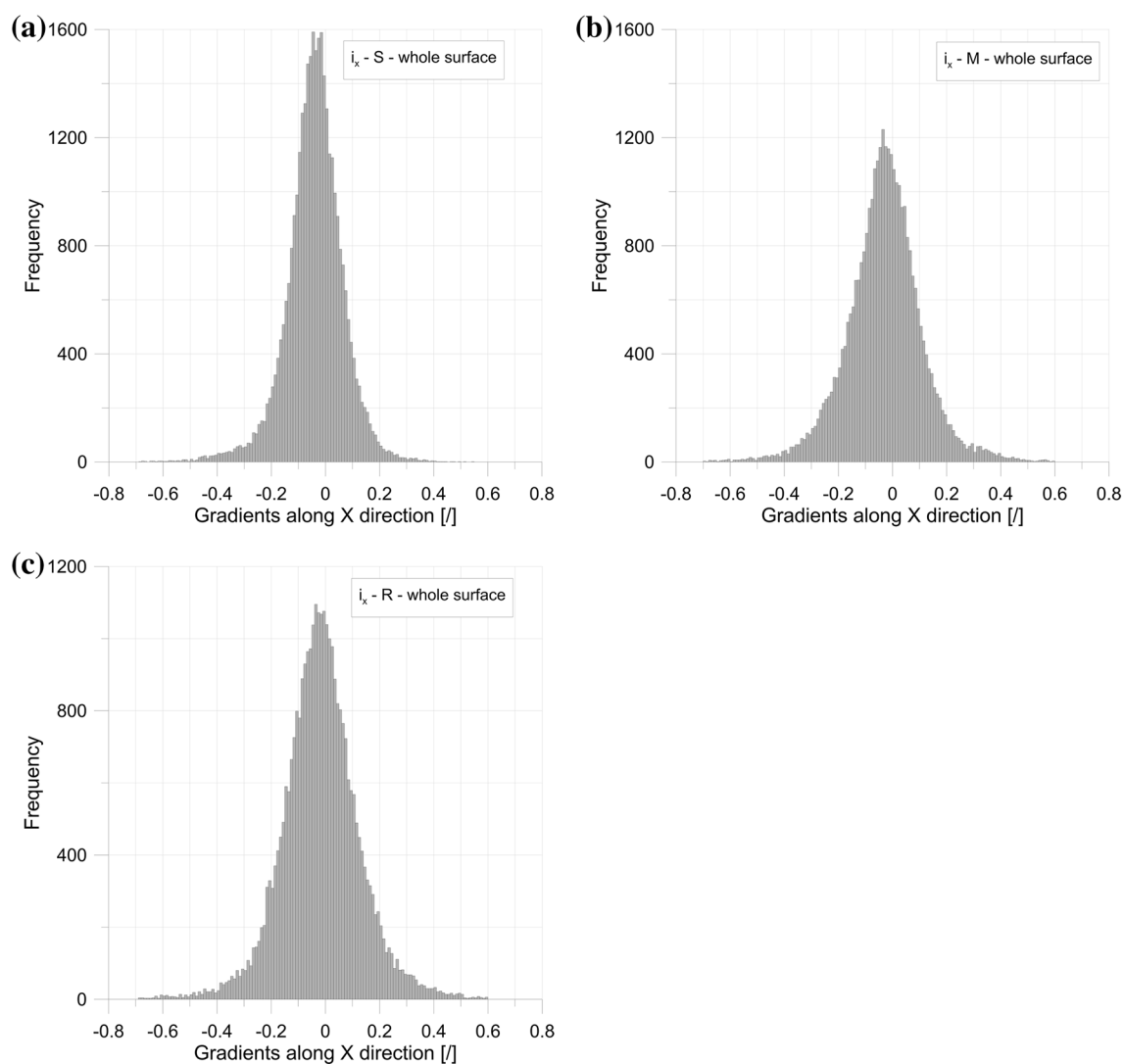


Fig. 11 Histograms of asperity gradients in the x direction for surface S (a), M (b) and R (c)

strength. Since any trace of the surface could be the seed trace, it is important to assess to what extent the outcome of the prediction depends on the selection of the seed trace. This will be covered in a later section.

5.4 Direct Shear Machines and Experimental Programme

The shear tests were conducted under normal stress values ranging from 0.1 to 6 MPa. Such a wide range required the use of two different apparatuses for a matter of load capacity and load control accuracy. A ShearTrac II direct shear machine from Geocomp was used for normal stresses below 1 MPa, while application of higher stresses was only possible with a Pro Lab shear machine (see Fig. 14a). The specimens were encased in metal boxes using high strength plaster (e.g. in Fig. 14b), as per revised ISRM suggested method (Muralha et al. 2013).

None of the devices could prevent rotation of the upper part of the specimen; however, tracking vertical displacements via three sensors placed on the loading plate showed that rotation of the upper wall remained below 2 degrees for all surfaces, which was considered acceptable.

Replicas of the three surfaces were tested under six values of normal stress and four shearing directions in order to assess anisotropy of the shear strength. The two shear machines offer different load control: the tests under low normal stress were conducted under constant normal force, while those under high normal stress were conducted under constant normal stress. This difference does not pose any issue for the validation of the model as long as the normal stress corresponding to the peak shear strength is clearly identified and used in the model.

As indicated in Eqs. (10) and (11), the residual shear strength can be predicted from the peak shear strength and the total sheared area at peak. It is therefore important to

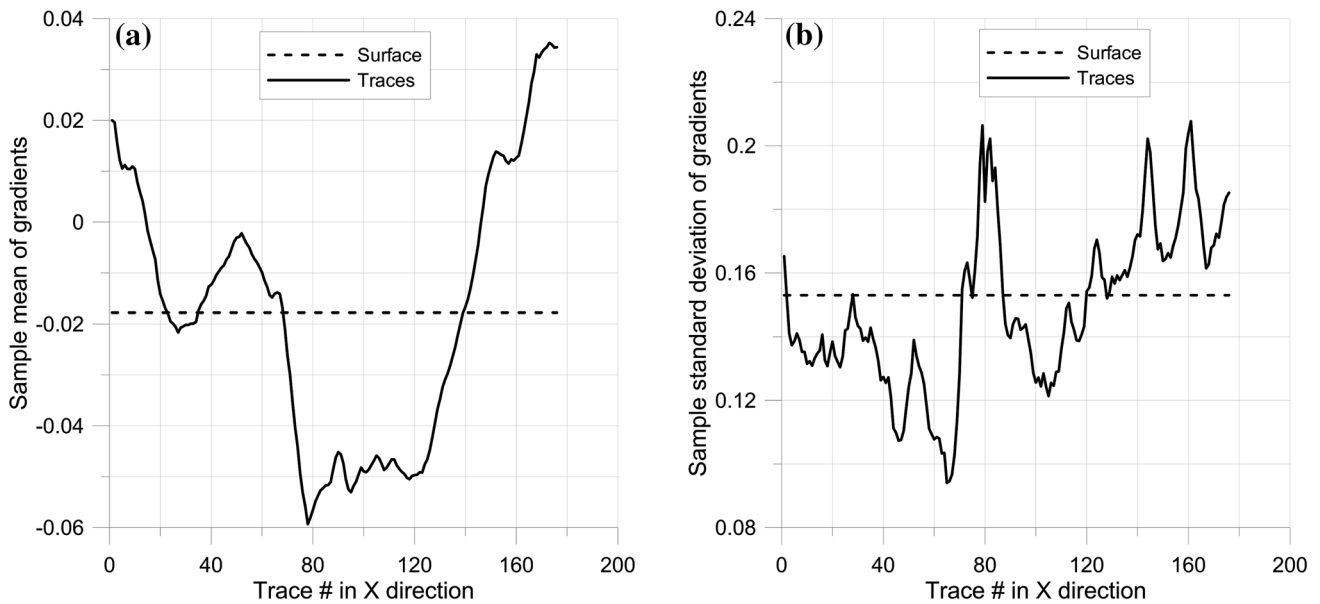


Fig. 12 Sample mean value (a) and standard deviation (b) of gradients along all traces in the x direction. The dashed lines represent the average of the sample means in (a) and of the sample standard deviations in (b), calculated in the x direction. Data pertain to surface R

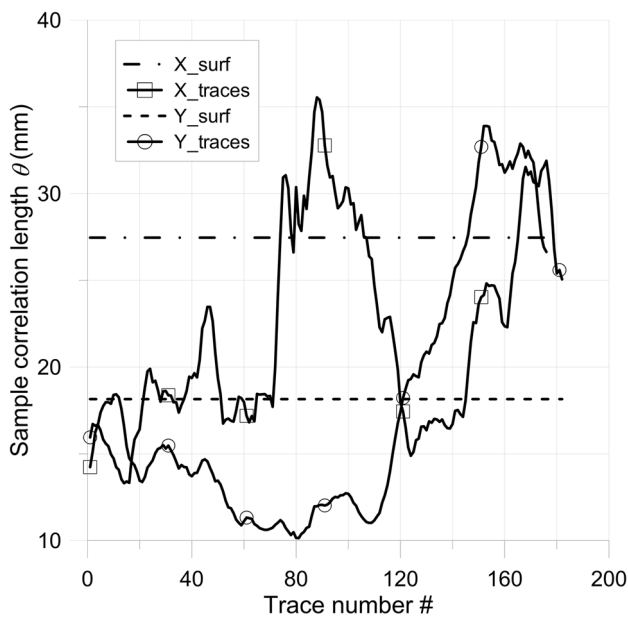


Fig. 13 Sample correlation length (θ) of each trace along directions x and y for surface R. The dashed lines represent the average correlation length of the sample over the whole surface along directions x and y

assess the capability of the model to properly capture surface degradation upon shearing. To do so, some tests have been conducted twice: once until the residual state (to obtain the residual strength) and once until the peak, for comparison with the model. Table 2 provides a summary of all tests performed.

6 Experimental Results and Validation of the Model

6.1 Experimental Results

This section first presents some of the experimental results before elaborating on the predictive capability of the new analytical model. Figure 15 presents the evolution of shear stress with tangential displacement for all three surfaces in the reference shearing direction (0°). Looking at the surface represented in Fig. 8 as the bottom wall of the discontinuity, the reference shearing direction, i.e. 0° , corresponds to the top part of the discontinuity moving downwards (towards decreasing numbers of the vertical— y axis).

The results are consistent with other results reported in the literature with an initial linear response, a peak reached after less than 5 mm of tangential displacement and a residual regime reached after 10–20 mm.

Figure 15d provides data regarding dilation upon shearing for surface M. For the sake of conciseness, not all the data are presented but all results are consistent with typical response of rock joints upon shearing: the higher the normal stress, the less dilation.

Figure 16 shows the same experimental results plotted in terms of shear stress-over-normal stress ratio. Again, the results are consistent with typical behaviour reported in the literature (Grasselli 2006). In particular, for each surface, the gap between the different curves narrows down as shearing progresses.

Fig. 14 **a** View of the Pro Lab shear machine load capacity of 100 kN. **b** View of the low part of a rock joint specimen encased in one of the steel boxes with plaster



Table 2 Summary of the experimental programme

Test type	Shearing direction (°)	Surface		
		S JRC = 2–4	M JRC = 8–10	R JRC = 16–18
CNF	0, 90, 180, 270	$\sigma_{no} = 0.1$ MPa	$\sigma_{no} = 0.1$ MPa	$\sigma_{no} = 0.1$ MPa
CNF		$\sigma_{no} = 0.3$ MPa	$\sigma_{no} = 0.2$ MPa	$\sigma_{no} = 0.2$ MPa
CNF		$\sigma_{no} = 0.6$ MPa	$\sigma_{no} = 0.4$ MPa	$\sigma_{no} = 0.4$ MPa
CN σ		$\sigma_n = 1.5$ MPa	$\sigma_n = 1.5$ MPa	$\sigma_n = 1.5$ MPa
CN σ		$\sigma_n = 3$ MPa	$\sigma_n = 3$ MPa	$\sigma_n = 3$ MPa
CN σ		$\sigma_n = 6$ MPa	$\sigma_n = 6$ MPa	$\sigma_n = 6$ MPa
CN σ		$\sigma_n = 1.5$ MPa	$\sigma_n = 1.5$ MPa	$\sigma_n = 1.5$ MPa
CN σ		$\sigma_n = 3$ MPa	$\sigma_n = 3$ MPa	$\sigma_n = 3$ MPa
CN σ		$\sigma_n = 6$ MPa	$\sigma_n = 6$ MPa	$\sigma_n = 6$ MPa

All tests conducted at shearing direction of 0, 90, 180 and 270 degrees at a rate of 0.5 mm/s

A total of 144 shear tests were conducted

CNF constant normal force, CN σ constant normal stress

Tests conducted until residual regime repeated until the peak are indicated in bold

6.2 Validation of the Model

This section focuses on the capability of the model to predict peak shear strength, surface degradation upon shearing and residual shear strength.

Figure 17 shows the comparison of predicted peak shear strength and measured shear strength for all three surfaces (S, M and R). Each sub-figure includes the results obtained for four shearing directions (identifiable by the symbols) and six normal stresses (identifiable by the magnitude of shear strength). The results show that the model can adequately predict the peak shear strength of the discontinuities tested, although the predictions seem to be more accurate at high values of normal stress. Figure 17d presents the cumulative frequency of relative error defined as $100 \times (\tau_{p\text{-predicted}} - \tau_{p\text{-exp}}) / \tau_{p\text{-exp}}$. A positive error reflects an over-prediction of shear strength and a negative value, an under-prediction. Figure 17d shows that one prediction is out by a factor of 2 (error just below 100%) but for 50% of the predictions, the relative error falls between -10 and

10%, which is acceptable. Figure 18 shows the comparison of the predicted and measured values of apparent friction (ratio of peak shear strength over normal stress) and also shows lines of constant relative error. Plotting the results in terms of apparent friction shows that the model tends to under estimate the peak shear strength for surfaces M and R. Note that large values of peak shear strength over normal stress are typically associated with the tests under low values of normal stresses. The exact reason why the model under-estimates the peak shear strength under low normal stress is not totally understood at this stage.

As discussed previously, prediction of residual shear strength relies on estimating the extent of sheared area. Figure 19 illustrates how increasing the normal stress results in a larger portion of the joint surface being sheared. The development of sheared areas is fully consistent with the location of steep facets of the original surface R, which is represented in Fig. 19d. Note that the model actually shears facets based on their apparent dip angle, which explains why steep facets located at the bottom of a valley are sheared

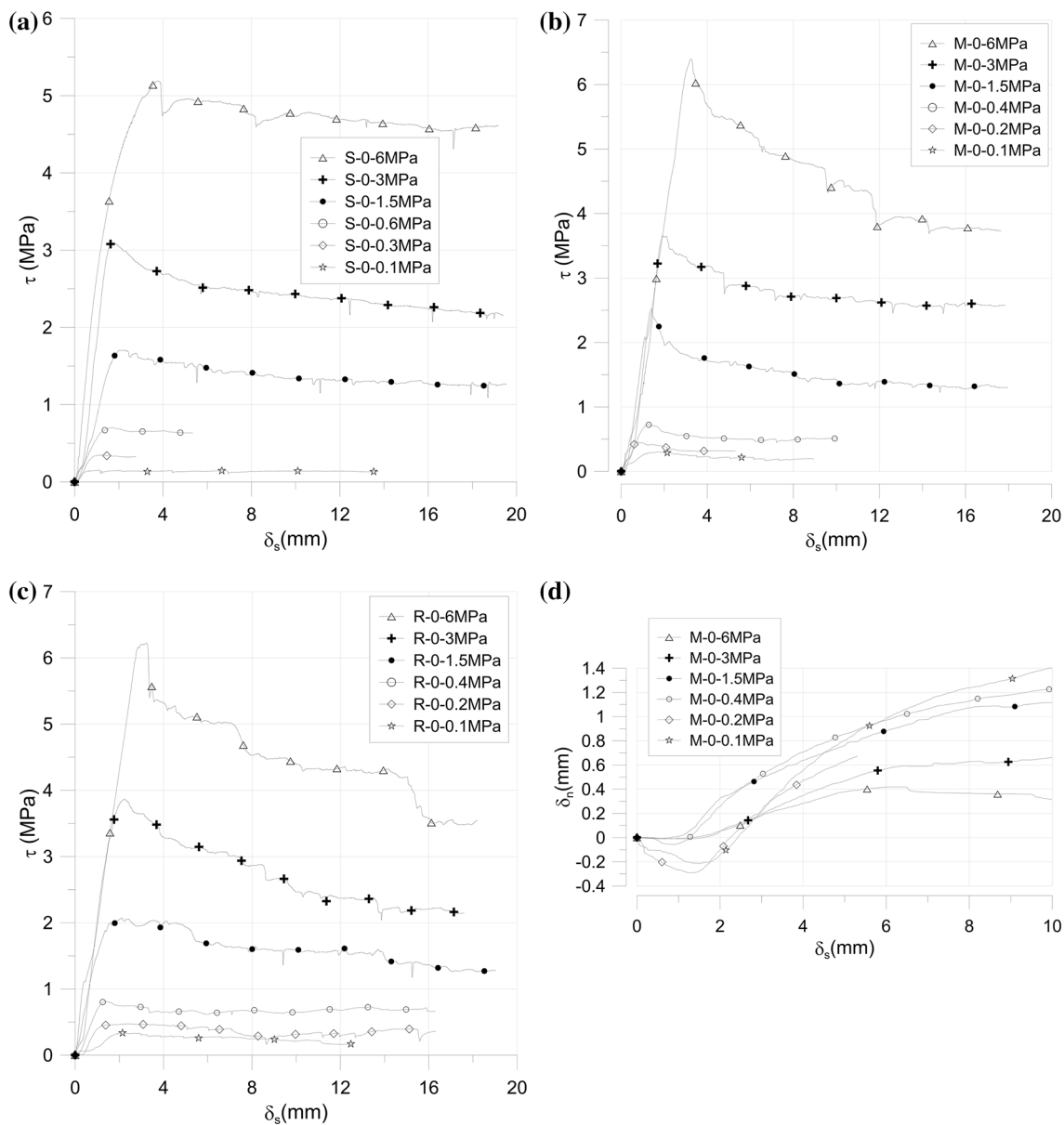


Fig. 15 Evolution of shear stress τ with tangential displacement δ_s for surfaces S (a), M (b) and R (c) under six different normal stresses. **d** Evolution of normal displacement δ_n with tangential displacement

δ_s during shearing for surface M under six different normal stresses. Tests conducted in the shearing reference direction (0°)

(points at $80 \text{ mm} < x < 100 \text{ mm}$, $55 \text{ mm} < y < 65 \text{ mm}$ in Fig. 19d). For a matter of space, not all details of surface degradation analysis are presented here.

In order to provide a more quantitative measure of the model ability to capture surface degradation, the difference between experimental surface and predicted surface post-shearing was estimated for all surfaces and four shearing directions. The results pertaining to surface R (the rougher and hence the more prone to degradation) are presented in Fig. 20 in terms of cumulative distribution of differences. Note that the surface comparison is made using experimental tests that were stopped just

after peak stress was reached (tests highlighted in bold in Table 1).

It can be seen that the majority of difference values fall within the range -1.5 to 1.5 mm with maximum recorded values of 3.2 and -4.7 mm . Such values are much larger than the measurement error (Fig. 9) and hence can be considered a reliable representation of the difference between model prediction and experiment, rather than a measurement inaccuracy.

Figure 20e shows the spatial distribution of the height difference between model and experiments for one test (surface R, sheared under 6 MPa of normal stress along

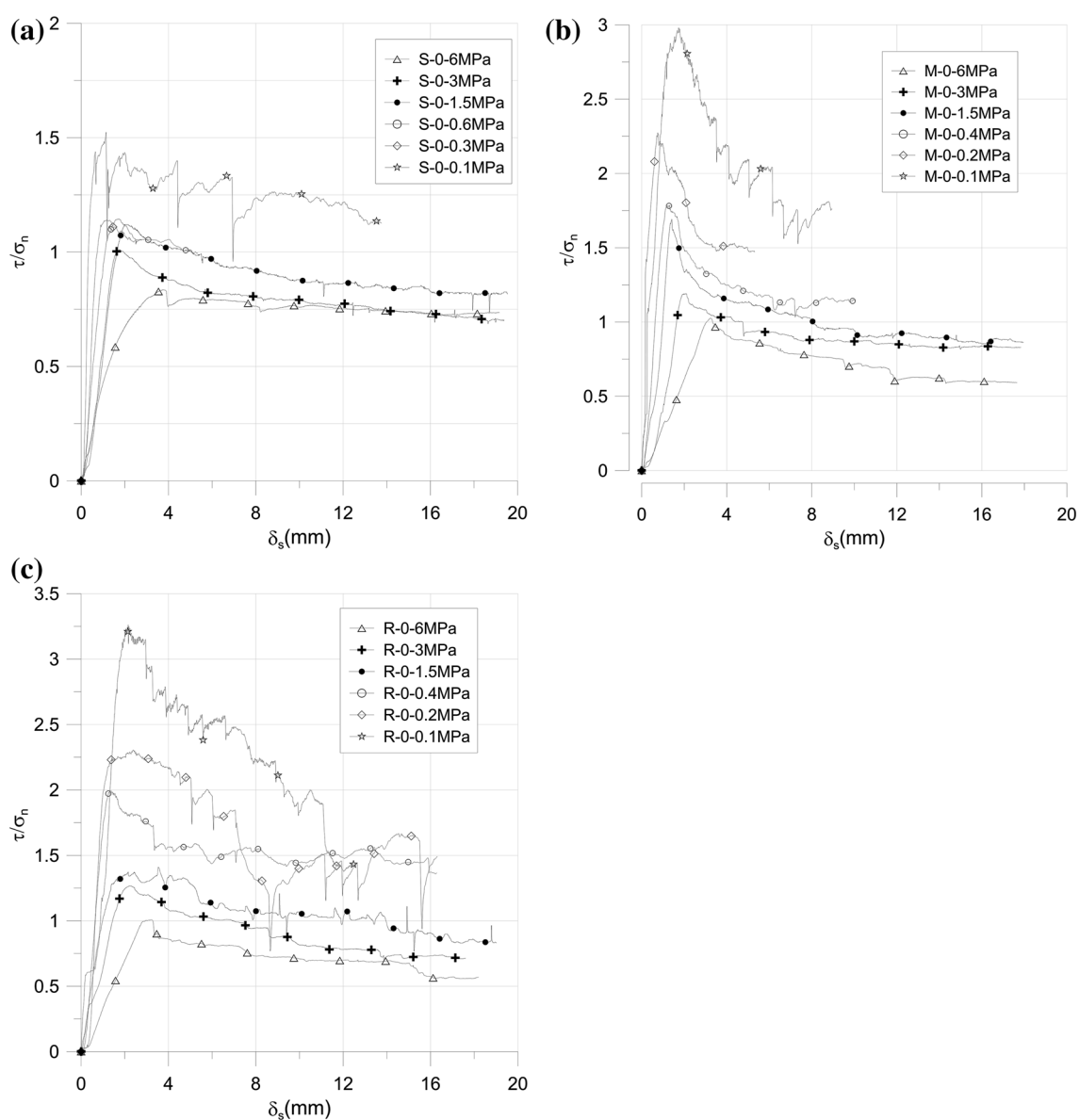


Fig. 16 Evolution of shear stress over normal stress (τ/σ_n) with tangential displacement δ_s for surfaces S (a), M (b) and R (c) under six different normal stresses. Tests conducted in the shearing reference direction (0°)

direction 0 degree). The high values of Δz seem to correspond to the edge of the specimen, which could be a reflection of local breakage occurring during testing, which results in $z_{\text{model}} > z_{\text{exp}}$. There is also a clear zone where the model under predicts asperity degradation ($z_{\text{model}} - z_{\text{exp}} \approx -2$ mm, in Fig. 20e). As discussed before, this is due to the fact that the model shears facets based on their apparent dip angle rather than location in a valley or a peak, which is what is normally observed in experiments (Hans and Boulon 2003).

Following the prediction of the peak shear strength and the extent of surface shearing, it is possible to estimate the residual shear strength using Eq. (11). Figure 21 shows a comparison of the predicted and measured residual shear strength for the

three surfaces under six normal stresses and for four shearing directions. With most of the data falling on or very close to the 1:1 line, it can be concluded that the model can adequately predict the residual shear strength of the surfaces. The maximum values of relative error are increased by about 15% compared to the distribution of errors pertaining to the peak shear strength. This is not surprising since the error on peak shear strength (Fig. 17d) is now combined to that made on the sheared surface morphology (Fig. 20).

Note that for a matter of space, the values of apparent friction (ratio of residual shear strength over normal stress) are not shown here but similar trends than those reported in Fig. 18 (i.e. an under-estimation of the apparent friction by the model) were observed for the residual strength.

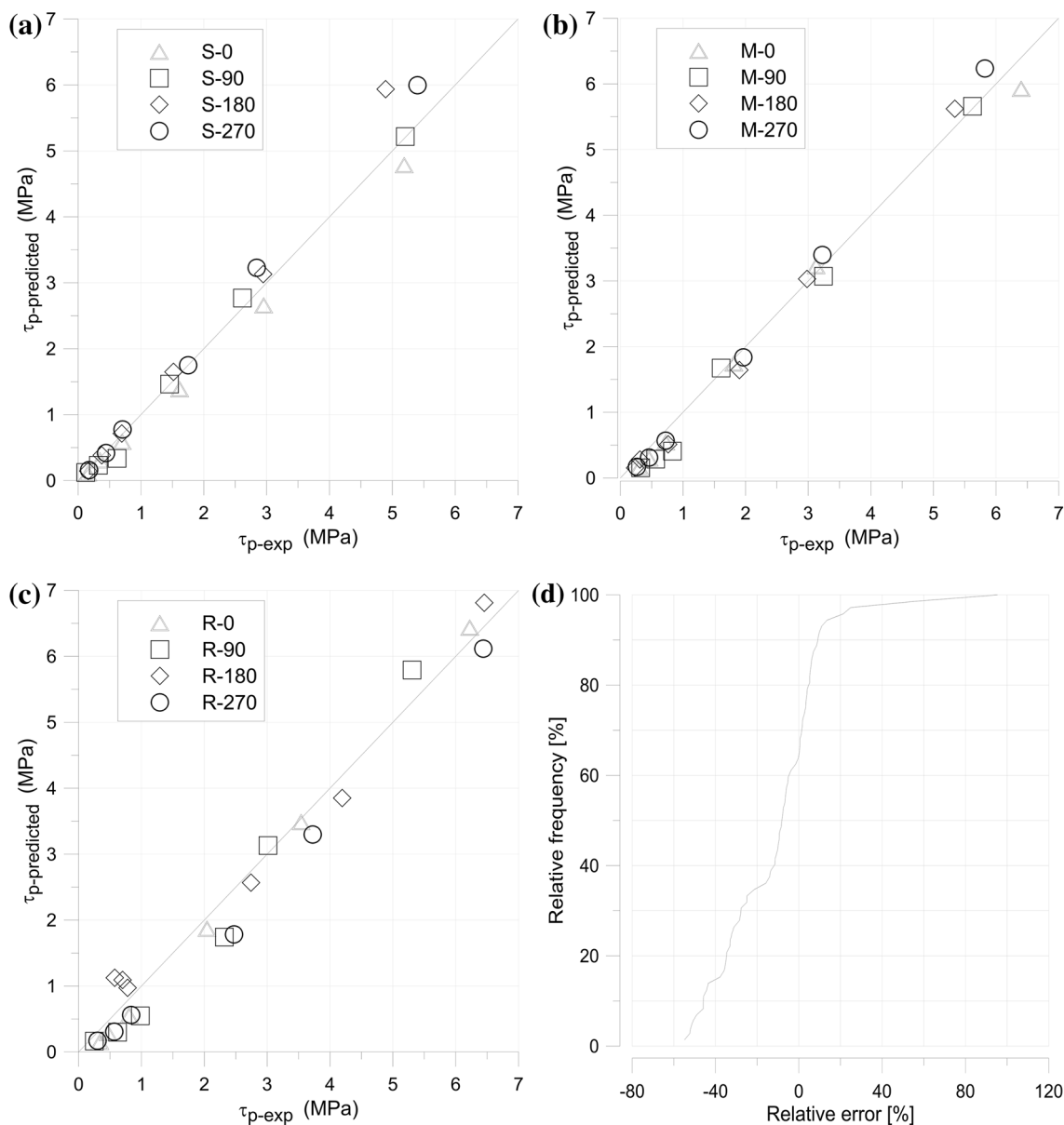


Fig. 17 Comparison of predicted peak shear strength ($\tau_{p\text{-predicted}}$) and measured peak shear strength ($\tau_{p\text{-exp}}$) for surface S (a), M (b) and R (c). The continuous line has a 1:1 gradient. **d** Cumulative distribution of

relative error for all three surfaces, four directions and six normal stresses. The relative error is calculated as $100 \times (\tau_{p\text{-predicted}} - \tau_{p\text{-exp}}) / \tau_{p\text{-exp}}$

6.3 Computational Time

Most FEM or DEM numerical models would require computational time of several hours to simulate shearing a 3D rough rock surface (see e.g. Lambert et al. 2010). The model presented in this paper can provide a reasonable estimate of peak shear strength, a sheared morphology (post-peak) and a residual strength in few seconds, which opens the door for stochastic analysis where a very large number of simulations are required.

In view of applying the model to larger surfaces in future, the evolution of computational time with the number of facets constituting the surface was assessed. To that end, the original

surfaces (made of about 65,000 facets) were halved (about 3000 facets) and doubled (about 120,000 facets). Simulations were run under several values of normal stresses. As expected, the more the facets, the higher the computational time (see Fig. 22a). With the current implementation of the model (in C sharp, running on a computer having the following characteristics: Intel(R) Core(TM) i7-4800MQ CPU @ 2.70 GHz, 8 GB of RAM), it can take up to 30 s for a surface made of 120,000 facets (Fig. 22b). The wide range of computational time for a given number of facets is related to the different values of normal stresses that result in different sheared geometry (see Fig. 19). In particular, focusing on the largest surface (120,000 facets), a clear correlation appears between

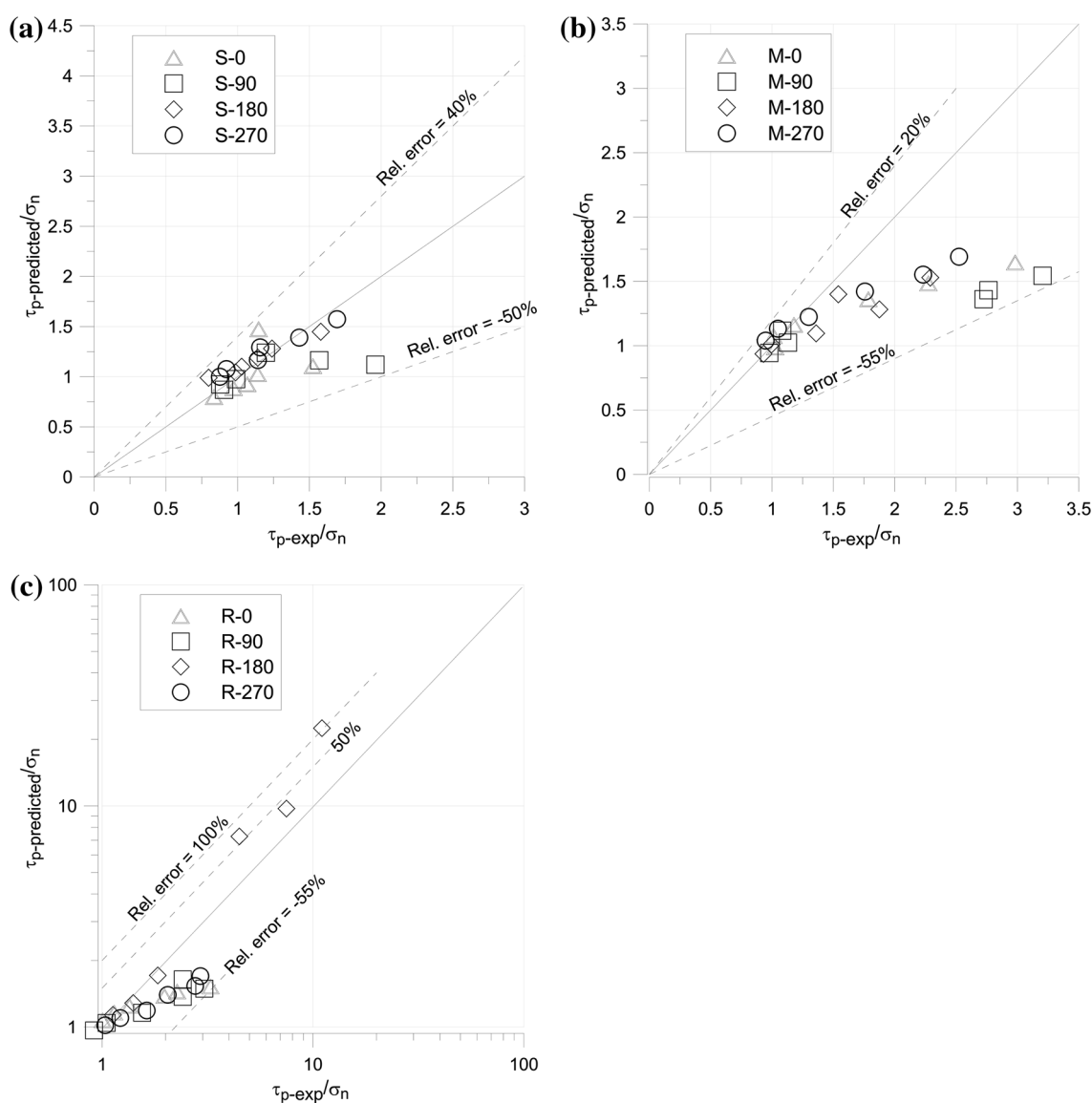


Fig. 18 Comparison of predicted peak shear strength over normal stress ($\tau_{p\text{-predicted}}/\sigma_n$) and measured peak shear strength over normal stress ($\tau_{p\text{-exp}}/\sigma_n$) for surface S (a), M (b) and R (c). The continuous

line has a 1:1 gradient, and the *dashed lines* provide values of relative error, calculated as $100 \times (\tau_{p\text{-predicted}} - \tau_{p\text{-exp}})/\tau_{p\text{-exp}}$

computational time and number of facets that have been sheared (Fig. 22b).

7 Validation of the Stochastic Approach for the Prediction of Discontinuity Shear Strength

7.1 Example of Synthetic Surface and Distribution of Shear Strength

An example of a random surface using statistics from surface R is displayed in Fig. 23. The two surfaces are clearly different, yet all surfaces created by the random

field model have statistical properties corresponding to those of the original surface. Figure 24 shows the distribution of heights and gradients of 25 simulations, which fall very close to Gaussian, as assumed.

Figure 25 shows the experimental results, the deterministic predictions (i.e. semi-analytical shear model applied to the original surfaces) and the predictions resulting from the stochastic approach (i.e. shear model applied to 100 synthetic surfaces, referred to as stochastic predictions). Note that only the results pertaining to surface R are presented, for the sake of conciseness. The surfaces simulated by the random field model are different enough to observe a wide range of responses. The difference between the highest and lowest shear strength is in the

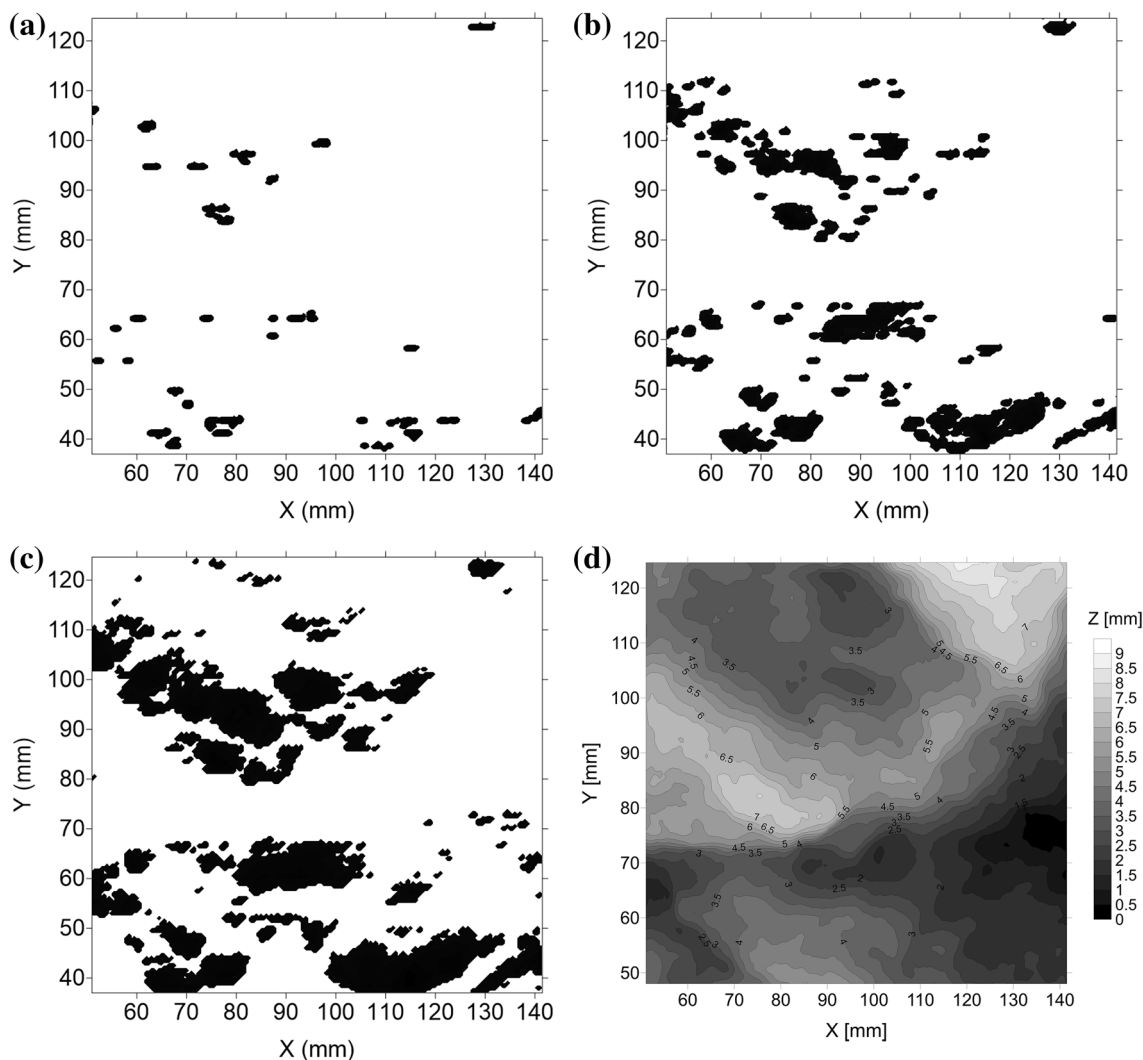


Fig. 19 Progressive surface degradation upon shearing predicted by the model under increasing level of normal stress: **a** 0.1 MPa, **b** 1.5 MPa, **c** 6 MPa. The *black pixels* represent the sheared facets.

order of 0.5 MPa under a normal stress of 6 MPa (Fig. 25a). All stochastic responses fall below their deterministic counterpart, but it will be demonstrated in a later section that this is a function of the correlation length. Focusing on the range of shear strength obtained under 6 MPa, Fig. 25b shows a well-graded cumulative distribution of peak and residual shear strength, from which can be calculated a mean value of shear strength (noted $\langle \tau_p \rangle$ —for peak strength or $\langle \tau_{res} \rangle$ —for residual strength).

7.2 Influence of the Number of Simulations

At this stage, it is important to ascertain how the distribution of shear strength evolves with the number of simulations. Figure 26 shows that using less than 100 simulations leads to fluctuations in the shear strength distributions. In contrast, with more than 100 simulations,

d Representation of the bottom wall of the original R surface. All dimensions in mm. Surface R sheared in the reference direction (0°), i.e. downwards along Y direction

changes in the shear distributions are negligible. Based on this finding, it was decided to use 100 simulated surfaces, for each prediction, in order to obtain reliable results in a reasonable time.

7.3 Influence of Correlation Length and Variance of Heights

As discussed in Sect. 4, the sample correlation length varies from trace to trace, posing the question of the representativity of the initial data set: in other words, which trace of the surface do we actually see in situ (e.g. in a cutting) and is it an adequate representation of the surface? To answer this question, it is critical to investigate the sensitivity of the shear strength distribution to the key variables used to construct the synthetic surfaces, namely the correlation length θ and the variance of height, σ_z^2 .

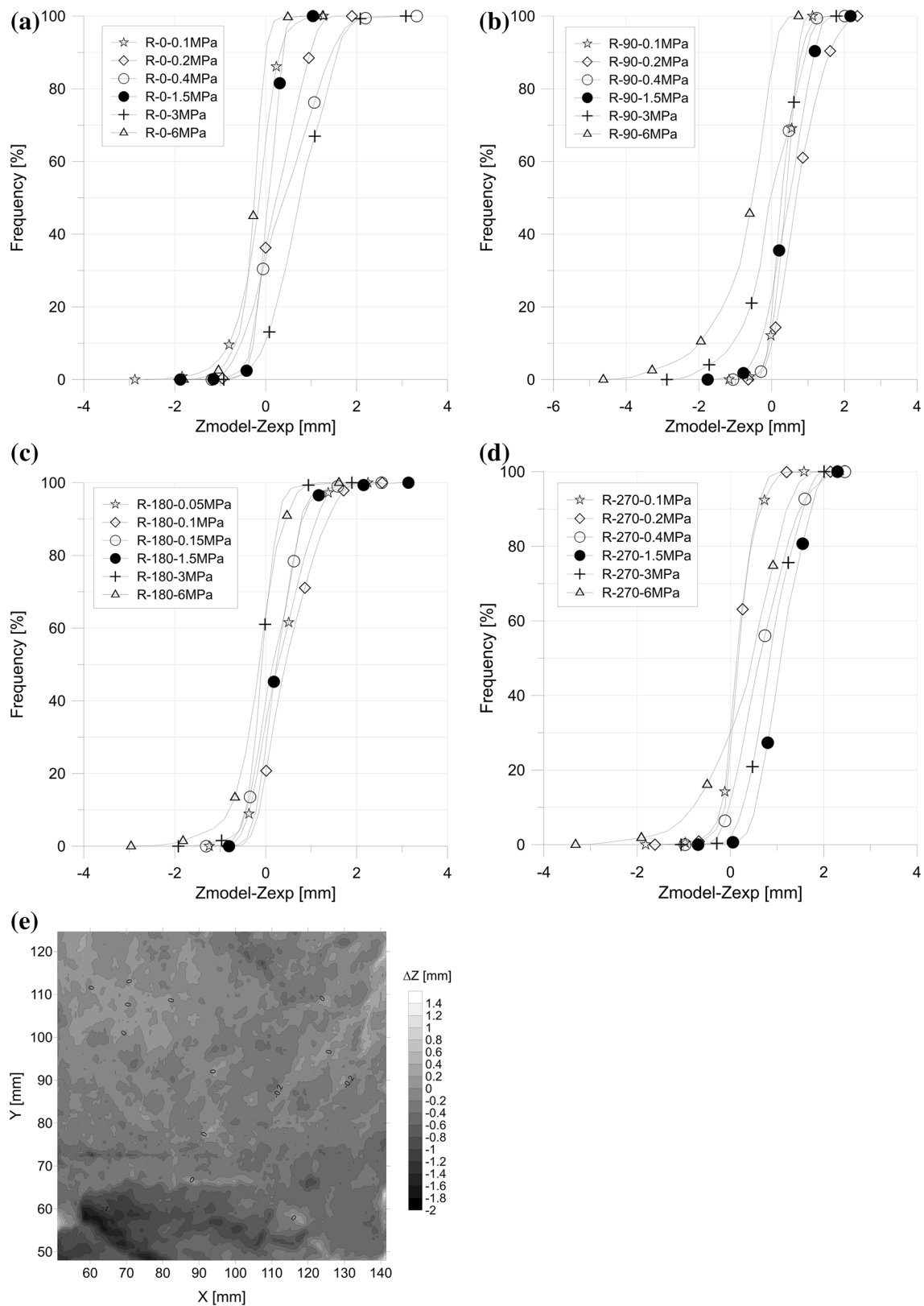


Fig. 20 Cumulative distribution of difference in height (z) between the model predictions and the experiments post-peak for surface PR under six values of normal stress. **a** At 0° , **b** at 90° , **c** at 180° , **d** at

270° . **e** Map of differences in height ($z_{\text{model}} - z_{\text{exp}}$) for surface R under 6 MPa sheared at 0° (along y axis, from *top* to *bottom*)

Figure 27 shows how the mean peak shear strength ($\langle \tau_p \rangle$) evolves with varying correlation and variance of heights. Note that each value of mean was calculated from 100 simulations and six different normal stresses were imposed on the surfaces. Figure 27a is obtained at constant height variance (equal to 2.8 mm^2) and Fig. 27b, at constant correlation length (equal to 27.4 mm). A value of 0.02 MPa was arbitrarily chosen as a lower bound for the normal stress. Figure 27a clearly demonstrates that a longer correlation length results in a lower peak shear strength, which is explained

by the fact that increasing the spatial correlation results in a smoother surface. Also very clear is the fact that the effect is more pronounced for low normal stresses: at 0.02 MPa, the relative decrease in shear strength is 60% (from 0.05 to 0.02 MPa), while it is only 3% at 6 MPa, over the range of correlation length considered.

The variance has been found to have an opposite effect: a larger variance yields a higher shear strength (Fig. 27b). Such observation can be interpreted as follows: a broader distribution of heights (i.e. a higher variance) means a rougher surface, which will provide a higher shear strength.

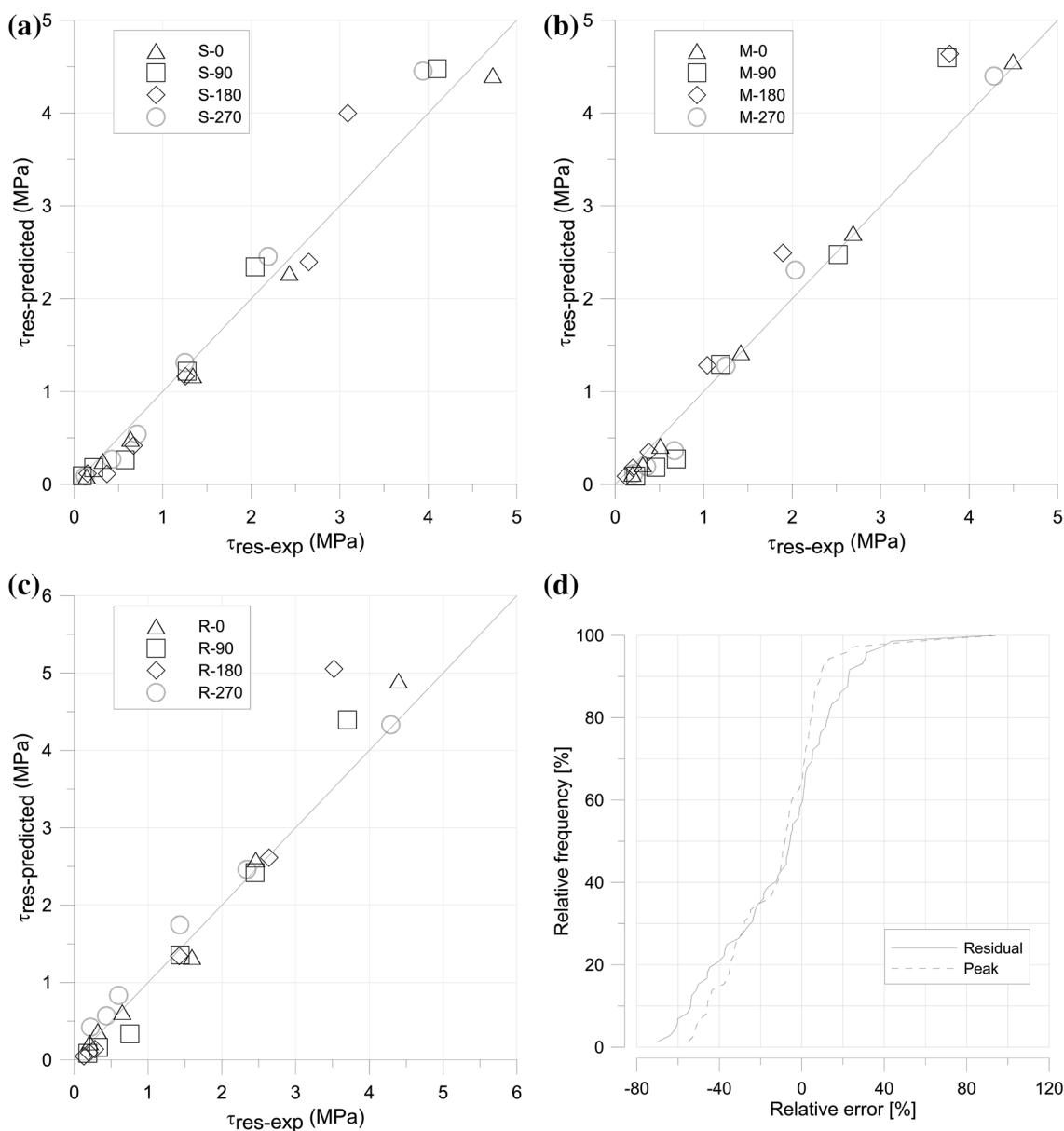


Fig. 21 Comparison of predicted residual shear strength ($\tau_{\text{res-predicted}}$) and measured residual shear strength ($\tau_{\text{res-exp}}$) for surface S (a), M (b) and R (c). The continuous line has a 1:1 gradient. d Cumulative

distribution of relative error for all three surfaces, four directions and six normal stresses. The relative error for the residual shear strength is calculated as $100 \times (\tau_{\text{res-predicted}} - \tau_{\text{res-exp}}) / \tau_{\text{res-exp}}$

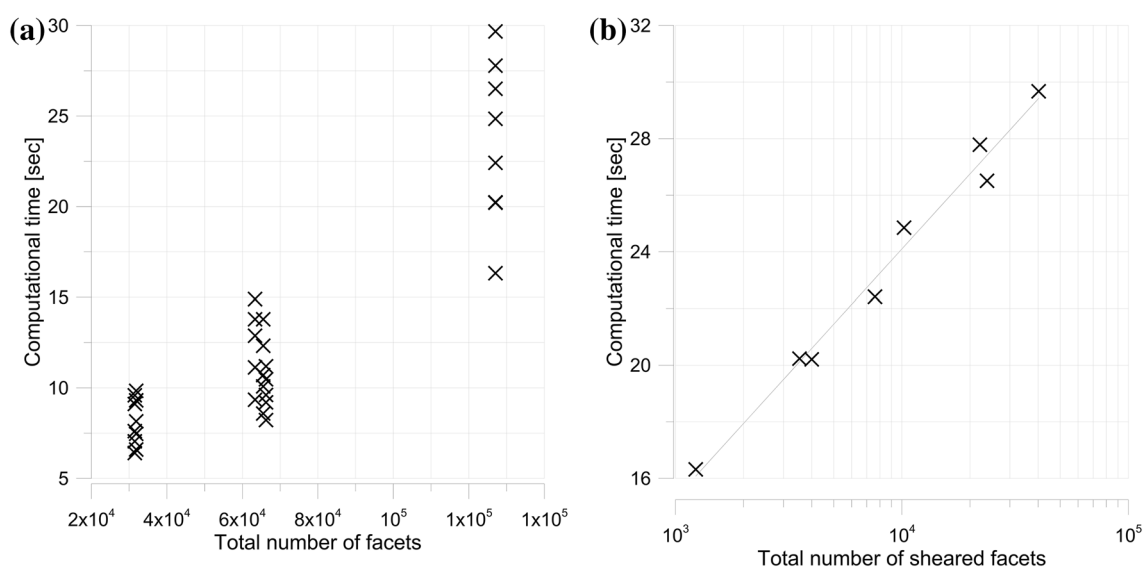


Fig. 22 **a** Evolution of computational time as a function of the total number of facets constituting the discontinuity surface. **b** Evolution of computational time as a function of total number of sheared facets for the largest surface under different normal stresses

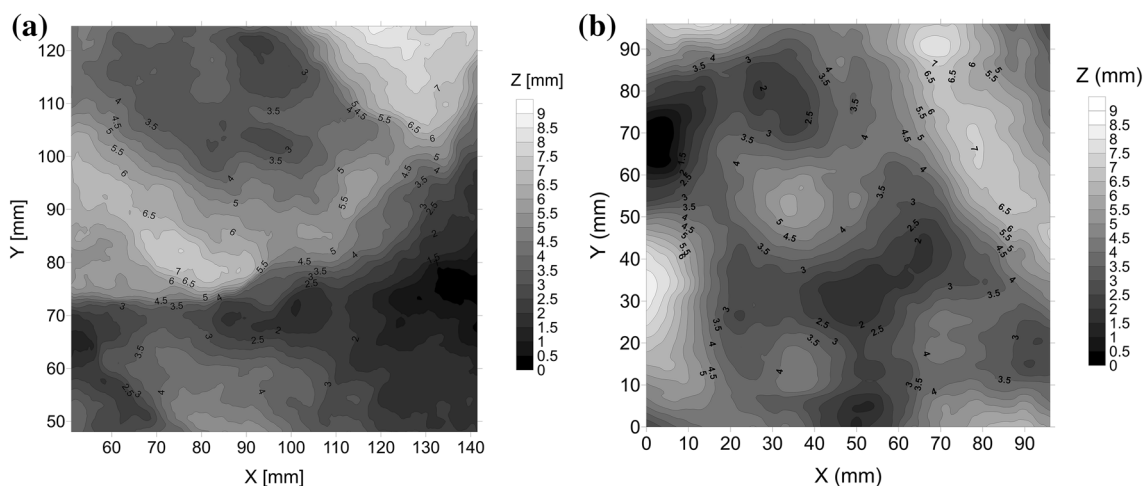


Fig. 23 Original surface R **(a)** and an example of a simulated surface **(b)** using the random field model and a correlation length of 27.4 mm and a variance of heights of 2.8 mm^2

Again, the effect is more pronounced under low normal stresses.

Following the findings of Fig. 27, a more detailed parametric study was conducted under a normal stress of 0.02 MPa, a value for which the sensitivity to correlation length and variance of height is the most pronounced. Twenty-five combinations of θ and σ_z^2 were considered, and for each one of them, 100 synthetic surfaces were created and the mean peak shear strength was obtained. The $(\theta, \sigma_z^2, \langle \tau_p \rangle)$ data were then used to create a contour map of $\langle \tau_p \rangle$ (by kriging) for varying correlation length and height variance (see Fig. 28a). The black dots represent the specific (θ, σ_z^2) points tested, while the contour lines correspond to the values of mean shear strength,

ranging from a minimum of 0.015 MPa to a maximum of about 0.110 MPa. Overall, the fluctuations in shear strength are quite modest across the values of correlation length and variance tested, except for variances larger than 3 mm^2 and correlation lengths lower than 18 mm (top left corner of the figure).

Interestingly, when superimposing the traces of the original surface R, represented by their actual values of (θ, σ_z^2) (crosses in Fig. 28b), on the contour map obtained in Fig. 28a, it appears that only a portion of the contour map is relevant for the considered surface. Although the parametric study (Fig. 28a) showed a possible variation of mean shear strength between 0.015 and 0.110 MPa, in case of surface R, the actual values of correlation length and

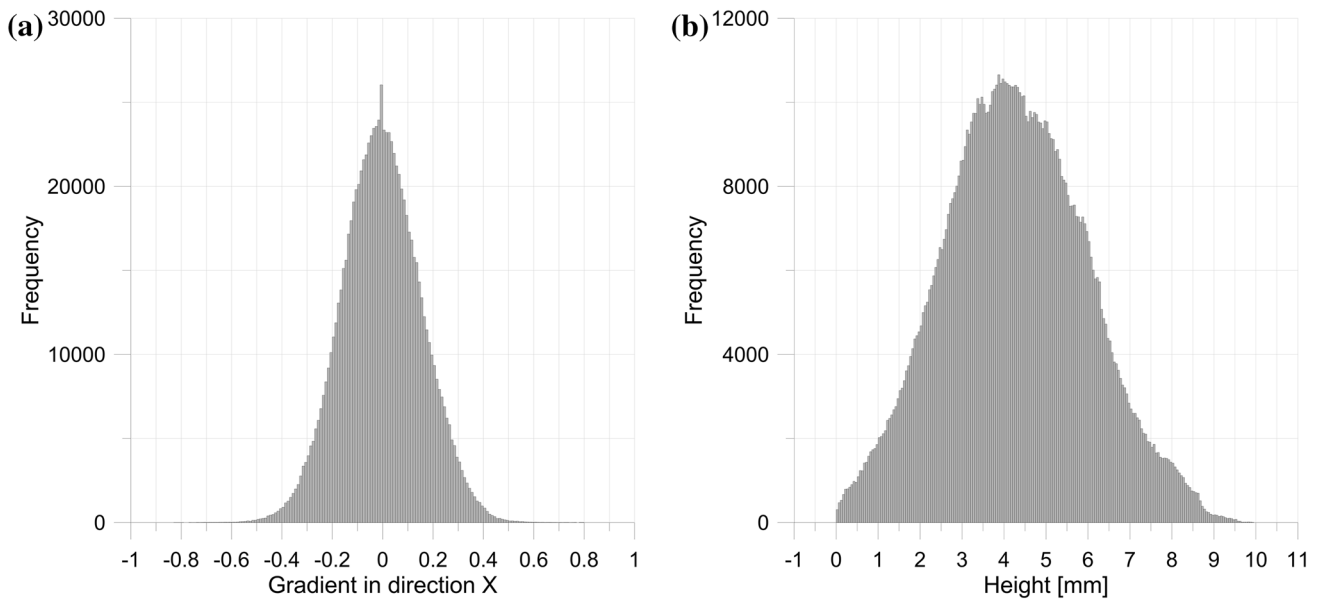


Fig. 24 Distribution of gradients (a) and surface height (b) of 25 synthetic surfaces

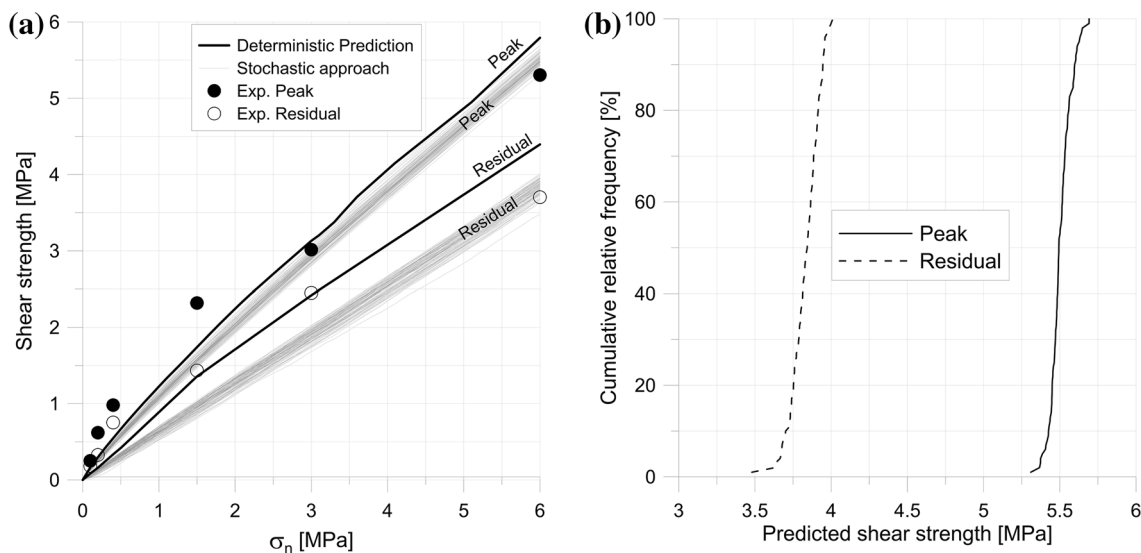


Fig. 25 a Peak and residual failure envelopes for surface R sheared along direction x . The *dots* represent experimental values, the *black lines* correspond to the prediction on the initial surface (referred to as deterministic), and the *grey lines* forming bands correspond to the

predictions on the virtual surfaces (referred to as stochastic). **b** Cumulative relative frequency of peak and residual shear strength under a normal stress of 6 MPa from which mean shear strength and standard deviation are calculated

height variance, calculated for all traces, reduce the range of mean shear strength to 0.024–0.036 MPa (Fig. 28b).

Considering now the mean peak shear strength corresponding to each cross of Fig. 28b and plotting the histograms of these values, it further appears that 53% of the data fall within the range 0.027–0.031 MPa with a mean value of 0.0295 MPa and a standard deviation of 0.0026 MPa (Fig. 29). Similar outcomes were obtained for surfaces S and M, although not presented here for a matter of conciseness.

Figures 28 and 29 suggest that, at least for the surfaces tested here, the uncertainty due to the selection of the seed trace is fairly limited (see Fig. 29).

7.4 Stochastic Modelling of Shear Strength

7.4.1 Predictions from the Statistics of the Whole Surface

In this section, the statistics of whole surfaces (S, M and R) were used as an input to the random field model (see

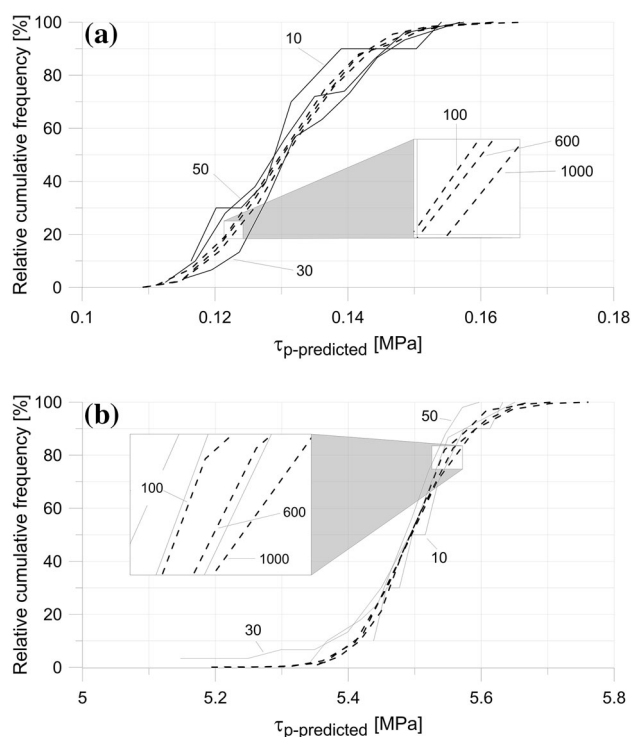


Fig. 26 Effect of the number of simulations on the cumulative distribution of predicted peak shear strength ($\tau_{p\text{-predicted}}$) for surface R sheared along direction x under a normal stress of 0.1 MPa (a) and 6 MPa (b). Continuous lines correspond to 10, 30 and 50 simulations, while dashed lines correspond to 100, 600 and 1000 simulations

Table 3). For each surface, 100 synthetic surfaces were created and virtually sheared.

Figure 30 shows that the mean value of shear strength (peak and residual) for all three surfaces compares reasonably well with the deterministic prediction obtained, for each surface, from the analytical model.

This clearly indicates that creating synthetic surface from the statistics of the whole surface yields satisfactory shear strength estimates. The next section will focus on synthetic surfaces created from the statistics of a seed trace, and the predictions from the stochastic approach will be compared to the experimental results.

7.4.2 Predictions from the Statistics of a Seed Trace

Here, 100 synthetic surfaces were created from a random seed trace of the natural surfaces S, M and R. These synthetic surfaces were virtually sheared under six values of normal stress using the semi-analytical model. For each value of normal stress, the mean value and standard deviation of both peak and residual shear strength were then calculated. Figure 31 shows the comparison of the results of the stochastic modelling to the experimental data obtained on the replicas of the three natural surfaces.

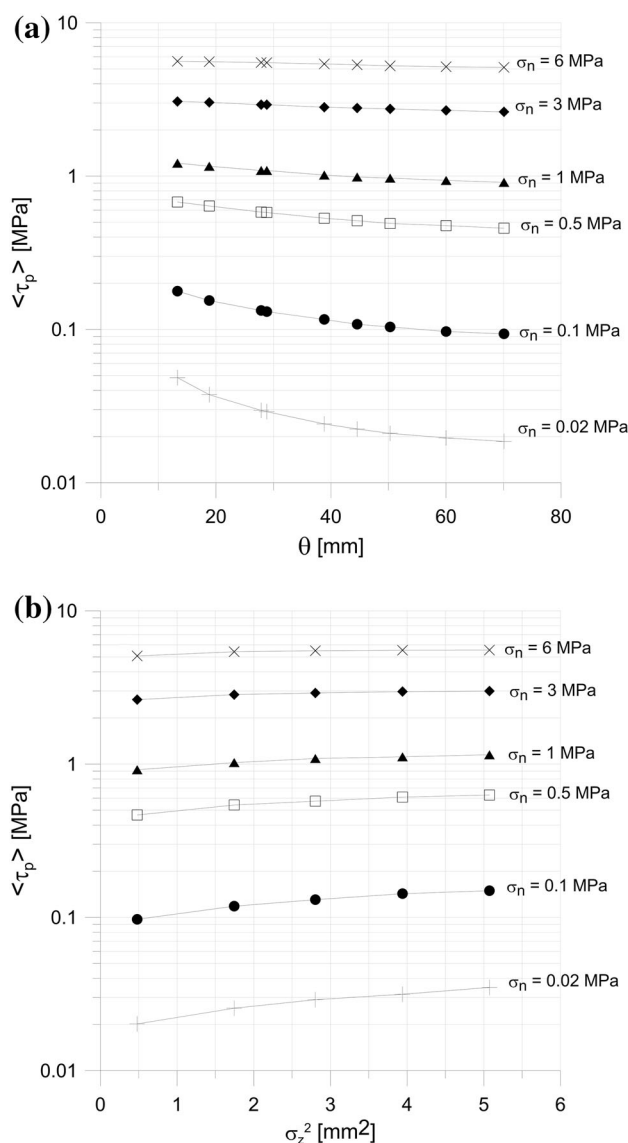


Fig. 27 Sensitivity of mean peak shear strength $\langle \tau_p \rangle$ to the correlation length θ at constant height variance σ_z^2 (equal to 2.8 mm^2) (a) and to the variance of heights σ_z^2 at constant correlation length θ (equal to 27.4 mm) (b). Random field statistics are obtained from surface R. Synthetic surfaces were sheared under six different values of normal stress along direction x

For the smoothest surface (S—Fig. 31a), four of the six predictions fall on the 1:1 line and two are slightly underestimated. The rougher the surface, the more the approach seems to underestimate the strength: three predictions are correct for surface M (Fig. 31b) but this falls to two correct predictions for surface R (Fig. 31c). For the other cases, the shear strength (peak and residual) is underestimated by a factor of 2, which means that the prediction is very conservative.

The under-estimation of shear strength is not caused by randomly creating surfaces from information available from a seed trace but is related to the quality of the semi-

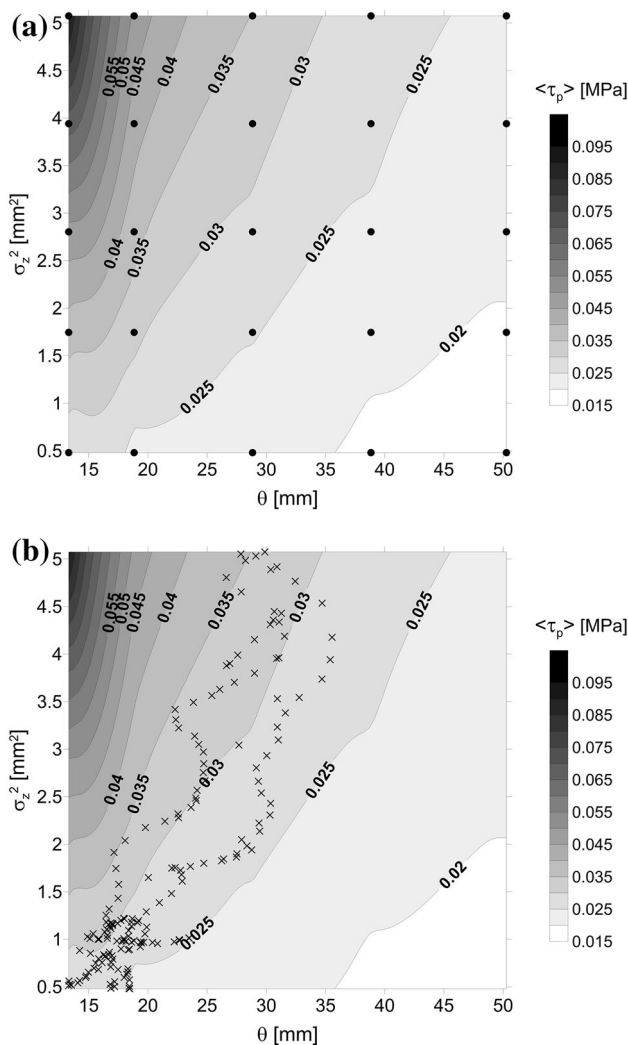


Fig. 28 **a** Contour plot of mean peak shear strength ($\langle \tau_p \rangle$) as a function of correlation length θ and variance of height (σ_z^2), for 100 synthetic surfaces sheared under a normal stress of 0.02 MPa. The black dots represent the combinations of θ and σ_z^2 tested. The contours map was obtained by kriging and using the $\langle \tau_p \rangle$ values obtained for each (θ , σ_z^2) combination. Contour lines are plotted at 0.005 MPa increments. **b** Plot of traces of surface R, represented by their actual combination of correlation length and variance of height (crosses) in the space of the contour map defined in Fig. 26a

analytical model for shear strength. Indeed, Fig. 32 clearly shows that the prediction of shear strength made on the original R surface closely matches the mean shear strength predicted by the stochastic approach.

Figure 31 shows the validation of the new approach detailed in Sect. 2 and which advocates that there is enough information contained in a single trace to create random surfaces and obtain a representative distribution of shear strength for the discontinuity. Indeed, the simulated values presented in Fig. 31 are all shear strength values of surfaces created from the statistics of seed traces only, not full surfaces.

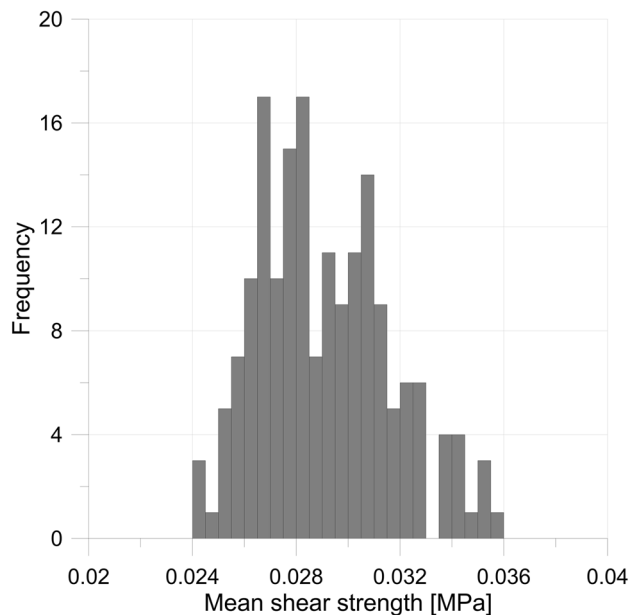


Fig. 29 Histogram of mean peak shear strength $\langle \tau_p \rangle$ where each value is calculated from 100 simulated surfaces created from each combination of (θ , σ_z^2) represented by the crosses in Fig. 28b

Table 3 Correlation length and variance of heights corresponding to the data set of the full surfaces S, M and R in the direction of shearing

	Surface S	Surface M	Surface R
Correlation length (mm)	38.7	26.2	27.4
Variance of heights (mm ²)	2.7	2.3	2.8

8 Conclusions

This paper presents a novel approach that could avoid any up-scaling exercise when estimating the shear strength of rock discontinuities by directly using the surface information available at the scale of the rock mass.

The first part of the paper deals with a new semi-analytical model that can predict the peak and residual shear strength of rock joints. This mechanistic model is inspired from the work of Huang et al. (2002) but has been significantly improved: the model handles real 3D surface, as opposed to 2D idealised ones (e.g. saw-tooth) and can predict both peak and residual strength. Also, the high precision in surface measurement implies that the facets are much smaller than the asperity size, which brings another level of complexity in the model and requires a strategy for progressive degradation. The model only requires the 3D description of the surface and the material strength properties to run; no calibration is necessary. At this stage, only a constant normal stress condition can be applied in the model and tangential displacements are not predicted, but this is not a problem for the newly proposed approach since

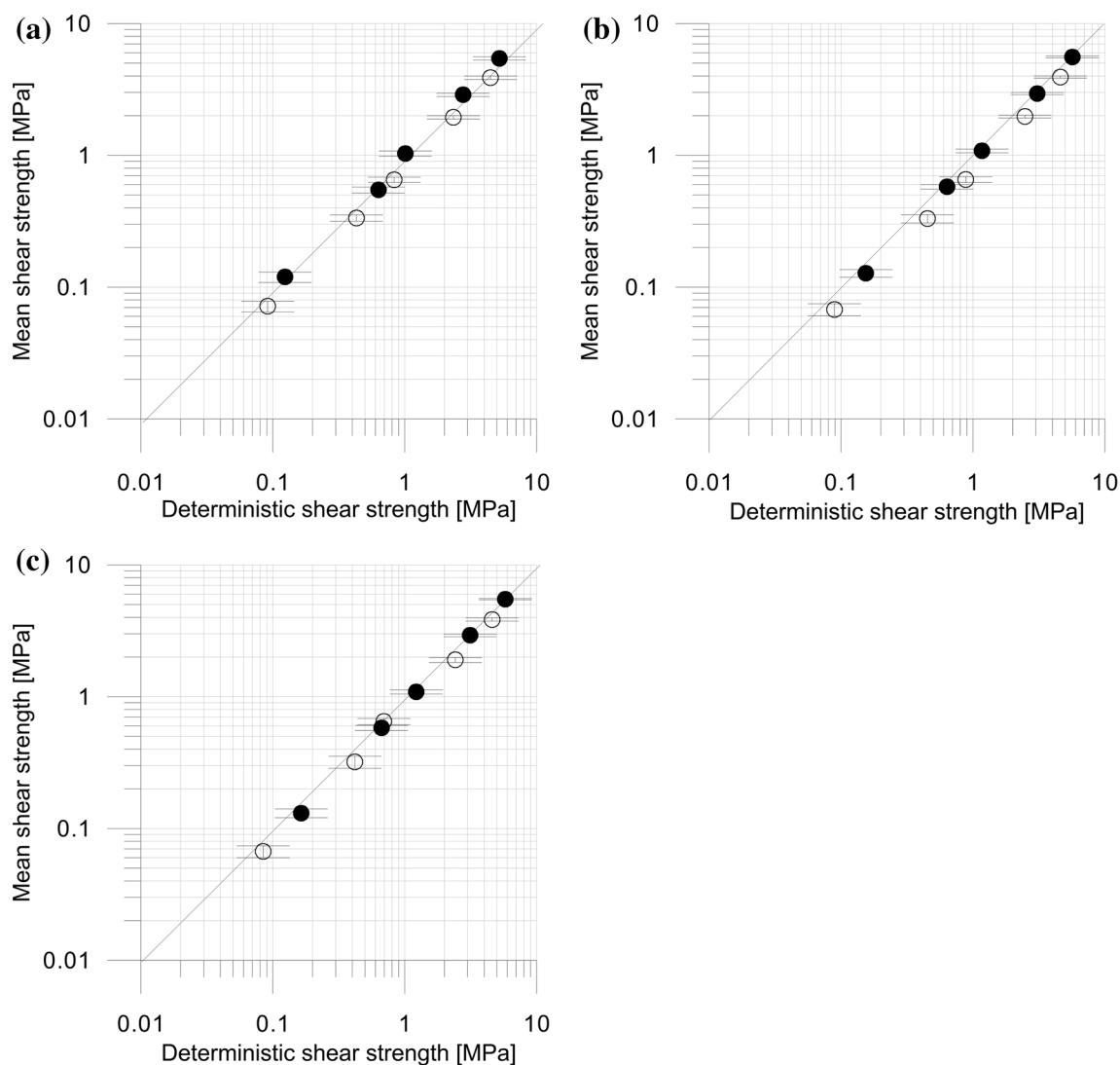


Fig. 30 Comparison between the mean value of shear strength, obtained by the stochastic approach, and deterministic predictions obtained from applying the semi-analytical model to surfaces S (a), M (b) and R (c). Shearing was done under normal stress values of 0.1,

0.5, 1, 3 and 6 MPa. *Full symbols* peak shear strength; *empty symbols* residual shear strength. The *error bar* shows the standard deviation associated with the mean value of shear strength

it is solely based on strength. A series of direct shear tests were conducted on replicas of three natural surfaces, under four shearing directions and under six levels of normal stress. The model was found to adequately predict both peak and residual shear strength under the set of conditions tested. However, validation was achieved with only three surfaces and more validation work will be conducted in future to better ascertain the predictive capability of the model, especially in the range of low normal stress. Unlike complex numerical models, this new model runs in a matter of seconds, which is ideal for the stochastic analyses that constitute the key point of the newly proposed approach to predicting shear strength.

The second part of the paper delves into the random field model required to produce and characterise

distributions of shear strength. A first analysis conducted with the statistics of whole surfaces showed that a minimum number of 100 simulations are recommended to obtain meaningful results. Then, a sensitivity analysis was conducted to assess the influence of correlation length and height variance on the distribution of shear strength. It was found that correlation length and variance of heights have opposite effects and that these effects are more relevant under low values of normal stress. Finally, peak and residual shear strengths of the three natural surfaces were predicted using the new approach. It was found that for high stresses and smooth surfaces, the predicted values of mean shear strength tend to match the experimental data but as the surface gets rougher and the normal stress drops, the mean

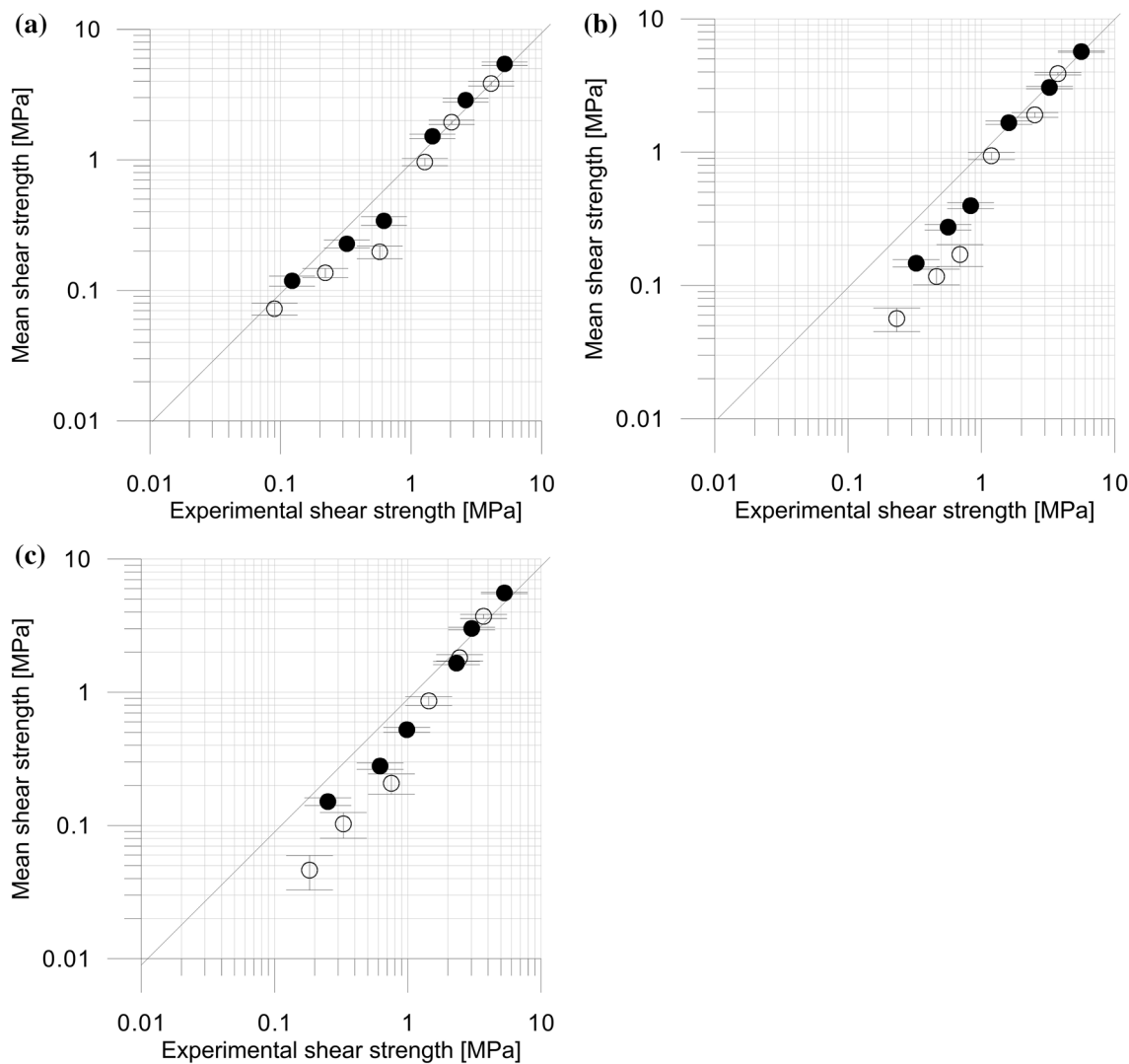


Fig. 31 Comparison of mean peak and residual shear strength resulting from stochastic modelling and experimental shear strength obtained for surface S. *Full symbols* peak shear strength; *empty symbols* residual shear strength. Hundred surfaces simulated from

values of predicted shear strength tend to fall below the measured values. However, it was shown that this underestimation can be due to the semi-analytical model for shear strength rather than the fact that synthetic surfaces were used. The significance of this research is that predicting the shear strength of a discontinuity could be achieved from information gathered directly at the discontinuity scale without having to resort to small specimens and hence to have to account for the scale effect. The method has not yet been applied to large in situ discontinuities, as this requires developments that are beyond the scope of this paper. Indeed, it is critical to account for possible opening, filling, weathering and persistence of discontinuities.

surface S (in **a** with $\sigma_z^2 = 3.21 \text{ mm}^2$ and $\theta = 40.1 \text{ mm}$), from surface M (in **b** with $\sigma_z^2 = 3.82 \text{ mm}^2$ and $\theta = 26.2 \text{ mm}$) and from surface R (in **c** with $\sigma_z^2 = 4.81 \text{ mm}^2$ and $\theta = 26.6 \text{ mm}$). Synthetic surfaces were virtually sheared under six values of normal stress

Acknowledgements The authors would like to acknowledge the financial contribution received from Pells Sullivan Meynink, Engineering Consultants, Sydney, and the help received from Dr. Mina Kardani for the implementation of the model.

Appendix A: Example of Calculation of Peak Shear Strength

This example focuses on the last two decrements (#154 and #155) of calculation of shear strength for the simplified surface shown in Fig. 33. Coordinates of the points making the geometry are given in Table 4. Note that the dimensions of the surface (6 m in the

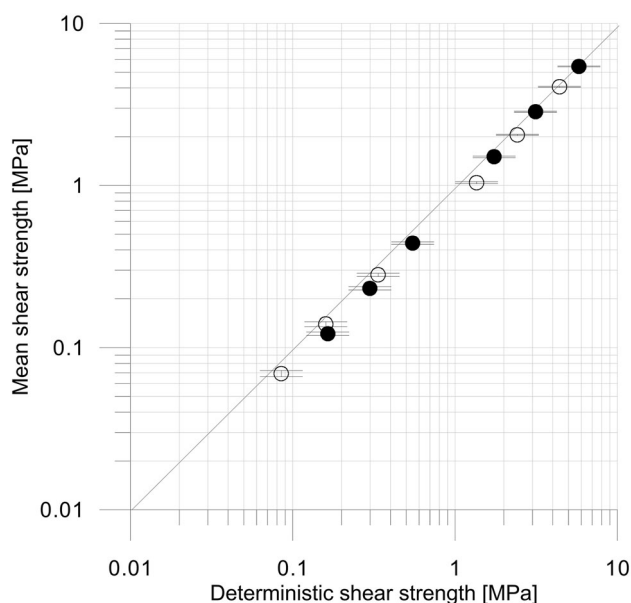


Fig. 32 Comparison of mean peak and residual shear strength resulting from stochastic modelling of 100 synthetic surfaces and shear strength prediction made from the original surface R. *Full symbols* peak shear strength; *empty symbols* residual shear strength. Hundred surfaces simulated using $\sigma_z^2 = 0.51 \text{ mm}^2$; $\theta = 13.3 \text{ mm}$ and sheared under six different values of normal stress

X direction by 1 m in the Y direction) and the material properties (Table 5) have been chosen to simplify the example and are not necessarily representative of the surfaces tested in this research. Shearing occurs along the X axis with the top wall moving from left to right. As a consequence, the gradient of the facets, as represented in Fig. 33, coincides with the apparent dip $\beta_{\text{app},i}$. Also, in order to simplify this example, the facets are not triangular but rectangular, which does not change the mechanics of the model. So, there are only six facets in the surface presented.

Fig. 33 Simplified surface geometry for an estimate of peak shear strength. The surface is made of six facets identified in the initial geometry (a). **b** Perspective view of the initial geometry showing the rectangular facets. Width of the surface (in Y direction): 1 m

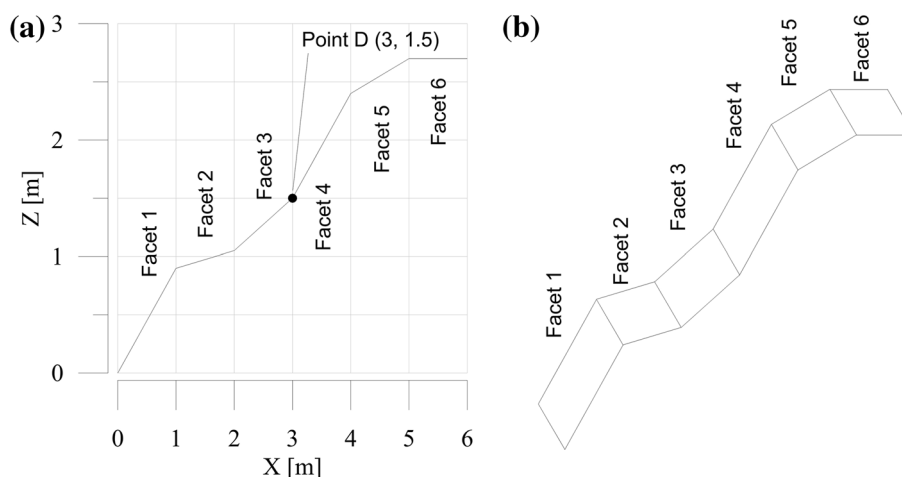


Table 4 Coordinates of the points of the initial geometry

Point	A	B	C	D	E	F	G
X (m)	0	1	2	3	4	5	6
Y (m)	0	0.9	1.05	1.5	2.4	2.7	2.7

Table 5 Dimensions, material properties and load

Surface dimensions	
l_x (m)	6
l_y (m)	1
Material parameters	
ϕ_b ($^\circ$)	28
ϕ ($^\circ$)	35
c (MPa)	0.2
Normal stress	
σ_n (MPa)	0.2
F_{macro} (kN)	1200

On the initial geometry, facets 1 and 4 are the steepest at 41.99° . The model sets the starting value of β^* at 41.9° (at the nearest 0.1° below the steepest facets), making facets 1 and 4 active from decrement #1.

At decrement 154, β^* has reduced to 26.6° (153 decrements of 0.1°). Following the progressive facet modification strategy described in Sect. 3.5, facets 2 and 5 have steepened and have become active. The apparent dip of all facets is reported in Table 6.

So, at decrement #154, four facets are active ($N_{\text{cf}} = 4$) and the total force applied to the discontinuity (1200 kN, see Table 4) is sheared between the four facets. Consequently, $f_{\text{local},i}$ is equal to 300 kN and $\sigma_{\text{local},i}$ is 0.3 MPa. Using Eqs. (7) and (6) and the materials properties reported in Table 5, the forces required to shear each facet at its

Table 6 Model variables at decrement 154

β_{app_i} (°)	26.6	26.6	24.23	26.6	26.6	8.52
β^* (°)	26.6					
A_i (m ²)	1.12	1.12	1.10	1.12	1.12	1.01
A_{ip} (m ²)	1	1	1	1	1	1
Facet active?	Yes	Yes	No	Yes	Yes	No
N_{cf} (# of active facets)	4					
f_{local_i} (N) (Eq. 4)	300,000	300,000	0	300,000	300,000	0
σ_{local_i} (Pa) (Eq. 5)	300,000	300,000	0	300,000	300,000	0
f_{shear_i} (kN) (Eq. 7)	410	410	0	410	410	0
$f_{sliding_i}$ (kN) (Eq. 6)	422	422	0	422	422	0
Outcome	Sheared	Sheared	n/a	Sheared	Sheared	n/a

Table 7 Model variables at decrement 155

β_{app_i} (°)	26.5	26.5	26.5	26.5	26.5	11.70
β^* (°)	26.5					
A_i (m ²)	1.12	1.12	1.12	1.12	1.12	1.02
A_{ip} (m ²)	1	1	1	1	1	1
Facet active?	Yes	Yes	Yes	Yes	Yes	No
N_{cf} (# of active facets)	5					
f_{local_i} (N) (Eq. 4)	240,000	240,000	240,000	240,000	240,000	0
σ_{local_i} (Pa) (Eq. 5)	240,000	240,000	240,000	240,000	240,000	0
f_{shear_i} (kN) (Eq. 7)	368	368	368	368	368	0
$f_{sliding_i}$ (kN) (Eq. 6)	336	336	336	336	336	0
Outcome	Sliding	Sliding	Sliding	Sliding	Sliding	n/a

base (f_{shear_i}) and to slide over it ($f_{sliding_i}$) are found to be 410 and 422 kN, respectively. Since $f_{shear_i} < f_{sliding_i}$, shearing takes place. This means that β^* is further reduced to 26.5°, which also becomes the new apparent dip (β_{app_i}) of all active facets.

As highlighted in Sect. 3.5, changing the apparent dip of facets 1, 2, 4 and 5 also affects the dip of facets 3 and 6 (see values in Table 7). In particular, we now have: $\beta_{app_3} = 26.69^\circ \geq \beta^* = 26.5^\circ$, meaning that facet 3 is now active and that $N_{cf} = 5$. Note that the apparent dip of facet 3 can be checked from the coordinates of point D in Fig. 33 (that still prevail at decrement 155), and the apparent dip of facets 1 and 2 at decrement 155 (26.5°).

The local normal stress drops from 0.3 MPa at decrement 154 to 0.24 MPa at decrement 155. As a result, the forces required to shear each facet at its base (f_{shear_i}) and to slide over it ($f_{sliding_i}$) become 368 and 336 kN, respectively. At that stage, the force required to slide over the facets is less than that required to shear them, which marks the end of the iterations.

The peak shear force is computed as the sum of the sliding force over all active facets at the last decrement:

$$f_{peak} = \sum_{i=1}^{N_{cf}} f_{sliding_i} = 5 \cdot 336 = 1840 \text{ kN}$$

The peak shear strength is calculated as:

$$\tau_{p\text{-predicted}} = f_{peak}/A_{tot} = 1.840 \text{ MN}/6 \text{ m}^2 \sim 0.31 \text{ MPa}$$

The residual shear strength is obtained by the following equation:

$$\tau_{res\text{-predicted}} = \frac{f_{peak} - c \cdot N_{cf} \cdot A_{ip}}{A_{tot}}$$

where $N_{cf} = 4$ (facet #3 became active but was not actually sheared). So we get:

$$\tau_{res\text{-predicted}} = \frac{1.84 - 0.2 \cdot 4 \cdot 1}{6 \cdot 1} = 0.17 \text{ MPa}$$

Figure 34 shows the final surface geometry after all steps of progressive shearing.

Appendix B: Derivation of Correlation Length θ

Consider points (x, y, z) of a surface and let us define $z(x, y)$ as the surface height at point (x, y) .

The directional gradients are defined as:

$$i_x = \frac{z(x + \Delta x, y) - z(x, y)}{\Delta x} \tag{14}$$

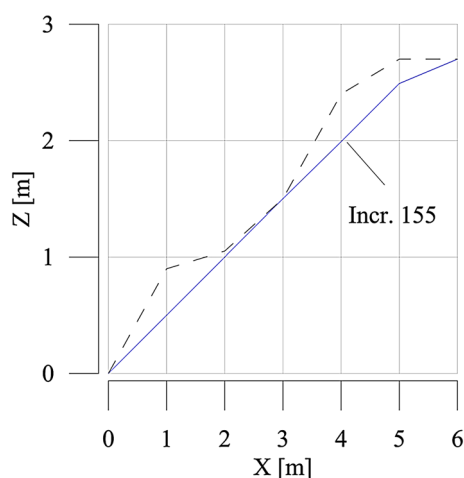


Fig. 34 Modified geometry at decrement 155 (final decrement). Dashed line shows the initial geometry, for comparison

$$i_y = \frac{z(x, y + \Delta y) - z(x, y)}{\Delta y} \quad (15)$$

For the sake of consistency with the equation presented in the core of the paper, let us consider one direction (either x or y) and drop the x or y subscript.

Using the definition of the gradients above, their variance $\text{var}[i]$ can be expressed as:

$$\text{var}[i] = \sigma_i^2 = \left(\frac{1}{\Delta x}\right)^2 \cdot \text{var}[z(x + \Delta x, y) - z(x, y)] \quad (16)$$

where σ_i is the standard deviation of gradients. Equation (16) then becomes:

$$\sigma_i^2 = \left(\frac{1}{\Delta x}\right)^2 \cdot [2 \cdot \sigma_z^2 - \text{cov}[z(x + \Delta x, y), z(x, y)]] \quad (17)$$

where cov is the covariance and σ_z is the standard deviation of heights, which are related by:

$$\text{cov}[z(x + \Delta x, y), z(x, y)] = \sigma_z^2 \cdot \rho(\Delta x) \quad (18)$$

Combining Eqs. (17) and (18), we get:

$$\sigma_i^2 = 2 \left(\frac{\sigma_z}{\Delta x}\right)^2 \cdot [1 - \rho(\Delta x)] \quad (19)$$

Equation (19) can be reformulated as:

$$\rho(\Delta x) = 1 - \frac{1}{2} \cdot \left(\frac{\sigma_i \cdot \Delta x}{\sigma_z}\right)^2 \quad (20)$$

A Gaussian correlation formulation was chosen for the correlation coefficient, which reads

$$\rho(d) = e^{-\pi \cdot \left(\frac{d}{\theta}\right)^2} \quad (21)$$

Combining Eqs. (20) and (21), in which the condition $d = \Delta x$ (where Δx is the spatial increment along the surface) is imposed, yields an estimate the correlation length θ

which depends on the standard deviation of the height and gradients:

$$\theta = \Delta x \cdot \sqrt{\frac{-\pi}{\ln\left(1 - \frac{1}{2} \left(\frac{\Delta x \cdot \sigma_i}{\sigma_z}\right)^2\right)}} \quad (22)$$

References

- Bahaaddini M, Sharrock G, Hebblewhite BK (2013) Numerical direct shear tests to model the shear behavior of rock joints. *Comput Geotech* 51:101–115
- Bandis S, Lumsden AC, Barton NP (1981) Experimental studies of the shear behaviour of rock joints. *Int J Rock Mech Min Sci* 18:1–21
- Bandis SC, Lumsden AC, Barton NR (1983) Fundamentals of rock joints deformation. *Int J Rock Mech Min Sci Geomech Abstr* 20(6):249–268
- Barton N (1976) Review of a new shear strength criterion for rock joint. *Eng Geol* 7:287–332
- Barton N (2013) Shear strength criteria for rock, rock joints, rockfill and rock masses: problems and some solutions. *J Rock Mech Geotech Eng* 5:249–261
- Barton N, Bandis S (1980) Some effects of scale on the shear strength of joints. *Int J Rock Mech Min Sci* 17:69–73
- Barton N, Choubey V (1977) The shear strength of rock joints in theory and practice. *Rock Mech* 10:1–54
- Barton N, Bandis S, Bakhtar K (1985) Strength, deformation and conductivity coupling of rock joints. *Int J Rock Mech Min Sci* 22(3):121–140
- Boulon M, Selvadurai APS, Benjelloun H, Feuga B (1993) Influence of rock joint degradation on hydraulic conductivity. *Int J Rock Mech Min Sci* 30:1311–1317
- Brady BHG, Brown ET (1985) *Rock mechanics for underground mining*. Springer, AA Dordrecht
- Brown SR (1987) Fluid flow through rock joints: the effect of surface roughness. *J Geophys Res* 92:1337–1347
- Carr JR, Warriner JB (1989) Relationship between the fractal dimension and joint roughness coefficient. *Bull Assoc Eng Geol XXVI(2):253–263*
- Cundall P (2000) Numerical experiments on rough joints in shear using a bonded model. In: *Aspects of tectonic faulting*, pp 1–9
- de Toledo PEC, de Freitas MH (1993) Laboratory testing and parameters controlling the shear strength of filled rock joints. *Géotechnique* 43(1):1–19
- Esaki T, Du S, Mitani Y, Ikusada K, Jing L (1999) Development of a shear-flow test apparatus and determination of coupled properties for a single rock joint. *Int J Rock Mech Min Sci* 36:641–650
- Fardin N, Stephansson O, Jing L (2001) The scale dependence of rock joint surface roughness. *Int J Rock Mech Min Sci* 38(5):659–669
- Fardin N, Feng Q, Stephansson O (2004) Application of a new in situ 3D laser scanner to study the scale effect on the rock joint surface roughness. *Int J Rock Mech Min Sci* 41:329–335
- Fenton GA (1990) *Simulation and analysis of random fields*, PhD thesis, Princeton University, p 178
- Fenton GA, Griffiths DV (2008) *Risk assessment in geotechnical engineering: technology and engineering*, Wiley, p 453
- Fenton GA, Vanmarcke E (1990) Simulation of random fields via local average subdivision. *J Eng Mech* 116(8):1733–1749
- Ferrero AM, Giani G (1990) Geostatistical description of the joint surface roughness. In: *Proceedings of the 31th U.S. symposium*

- on rock mechanics (USRMS), Golden, Colorado, paper ARMA-90-0463
- Gale JE (1982) Assessing the permeability characteristics of fractured rocks. *Geol Soc Am Spec Pap* 189:163–182
- Gens A, Carol I, Alonso E (1990) A constitutive model for rock joints formulation and numerical implementation. *Comput Geotech* 9(1–2):3–20
- Giacomini A, Buzzi O, Giani G, Migliazza M, Ferrero A (2008) Numerical study of flow anisotropy within a single natural joint. *Int J Rock Mech Min Sci* 45:47–58
- Goodman R (1989) *Introduction to rock mechanics*. Springer, AA Dordrecht
- Grasselli G (2006) Shear strength of rock joints based on quantified surface description. *Rock Mech Rock Eng* 39(4):295–314
- Grasselli G, Eger P (2003) Constitutive law for the shear strength of rock joints based on three-dimensional surface parameters. *Int J Rock Mech Min Sci* 40(1):25–40
- Grasselli G, Lisjak A, Mahabadi OK, Tatone BS (2014) Influence of pre-existing discontinuities and bedding planes on hydraulic fracturing initiation. *Eur J Environ Civ Eng* 19(5):580–597
- Haberfield CM, Johnston IW (1994) A mechanistically-based model for rough rock joints. *Int J Rock Mech Min Sci* 31(4):279–292
- Hans J, Boulon M (2003) A new device for investigating the hydro-mechanical properties of rock joints. *Int J Numer Anal Meth Geomech* 27(6):513–548
- Huang TH, Chang CS, Chao CY (2002) Experimental and mathematical modeling for fracture of rock joint with regular asperities. *Eng Fract Mech* 69(17):1977–1996
- Hutson RW, Dowing CH (1990) Joint asperity degradation during cyclic shear. *Int J Rock Mech Min Sci* 27(2):109–119
- Indraratna B, Ranjith P (2001) *Hydromechanical aspects and unsaturated flow in jointed rock*. A.A. Balkema Publisher, Amsterdam
- Indraratna B, Haque A, Aziz N (1998) Laboratory modelling of shear behaviour of soft joints under constant normal stiffness condition. *Geotech Geol Eng* 16(1):17–44
- Indraratna B, Premadasa W, Brown ET, Gens A, Heitor A (2014) Shear strength of rock joints influenced by compacted infill. *Int J Rock Mech Min Sci* 70:296–307
- Johnston IW, Kodikara JK (1994) Shear behaviour of irregular triangular rock-concrete joints. *Int J Rock Mech Min Sci* 31(4):313–322
- Karami A, Stead D (2008) Asperity degradation and damage in the direct shear test: a hybrid FEM/DEM approach. *Rock Mech Rock Eng* 41(2):229–266
- Koyama T, Fardin N, Jing L, Stephansson O (2006) Numerical simulation of shear-induced flow anisotropy and scale-dependent aperture and transmissivity evolution of rock fracture replicas. *Int J Rock Mech Min Sci* 43(1):89–106
- Krumbholz M, Hieronymus C, Burchardt S, Troll V, Tanner D, Friese N (2014) Weibull-distributed dyke thickness reflects probabilistic character of host-rock strength. *Nat Commun*. doi:10.1038/ncomms4272
- Ladanyi B, Archambault G (1977) Shear strength and deformability of filled indented joints. In: *Proceedings of international symposium on the geotechnics of structurally complex formations*. Capri, pp 317–326
- Lambert C, Buzzi O, Giacomini A (2010) Influence of calcium leaching on the mechanical behavior of a rock-mortar interface: a DEM analysis. *Comput Geotech* 37(3):258–266
- Lambert C, Thoeni K, Giacomini A, Casagrande D, Sloan SW (2012) Rockfall hazard analysis from discrete fracture network modelling with finite persistence discontinuities. *Rock Mech Rock Eng* 45(5):871–884
- Lanaro F (2000) A random field model for surface roughness and aperture of rock fractures. *Int J Rock Mech Min Sci* 37(8):1195–1210
- Lee HS, Cho TF (2002) Hydraulic characteristic of rough fractures in linear flow under normal and shear load. *Rock Mech Rock Eng* 35(4):299–318
- Li Y, Oh J, Mitra R, Canbulat I (2016) A fractal model for the shear behaviour of large-scale opened rock joints. *Rock Mech Rock Eng*. doi:10.1007/s00603-016-1088-8
- Marache A, Riss J, Gentier S, Chiles JP (2002) Characterization and reconstruction of a rock fracture surface by geostatistics. *Int J Numer Anal Methods Geomech* 26(9):873–896
- Muralha J, Grasselli G, Tatone B, Blumel M, Chryssanthakis P, Yujing J (2013) ISRM suggested method for laboratory determination of the shear strength of rock joints: revised version. In: Ulusay R (ed) *The ISRM suggested methods for rock characterization, testing and monitoring: 2007–2014*, Wiley, pp 131–142. doi:10.1007/978-3-319-07713-0
- Noorian-Bidgoli M, Jing L (2015) Stochastic analysis of strength and deformability of fractured rocks using multi-fracture system realizations. *Int J Rock Mech Min Sci* 78:108–117
- Patton FD (1966) Multiple modes of shear failure in rock. In: *Proceeding of first congress of ISRM, Lisbon, Portugal, vol 1*, pp 509–513
- Plesha ME (1987) Constitutive models for rock discontinuities with dilatancy and surface degradation. *Int J Numer Anal Meth Geomech* 11(4):345–362
- Raven RG, Gale JE (1985) Water flow in a natural rock fracture as a function of stress and sample size. *Int J Rock Mech Min Sci* 22(4):251–261
- Seidel JP, Haberfield CM (1995) The use of fractal geometry in a joint shear model. In: *Mechanics of jointed and faulted rock: proceedings of the 2nd international conference on mechanics of jointed and faulted rock, MJFR-2, Vienna, Austria*, pp 529–534
- Seidel JP, Haberfield CM (2002) A theoretical model for rock joints subjected to constant normal stiffness direct shear. *Int J Rock Mech Min Sci* 39(5):539–553
- Selvadurai APS, Yu Q (2005) Mechanics of a discontinuity in a geomaterial. *Comput Geotech* 32(2):92–106
- Tse R, Cruden CM (1979) Estimating joint roughness coefficient. *Int J Rock Mech Min Sci* 16(5):303–307
- Vallier F, Mitani Y, Boulon M, Esaki T, Pellet F (2010) A shear model accounting scale effect in rock joints behaviour. *Rock Mech Rock Eng* 43:581–595
- Vanmarcke E (1983) *Random fields: analysis and synthesis*. The MIT press, Cambridge, MA, pp 382
- Witherspoon PA, Wang JSY, Iwai K, Gale JE (1980) Validity of cubic law for fluid flow in a deformable rock fracture. *Water Resour Res* 16(6):1016–1024
- Xu C, Dowd PA (2014) Stochastic fracture propagation modelling for enhanced geothermal systems. *Math Geosci* 46(6):665–690
- Yang J, Rong G, Hou D, Peng J, Zhou C (2016) Experimental study on peak shear strength criterion for rock joints. *Rock Mech Rock Eng* 49(3):821–835
- Zandarin MT, Alonso E, Olivella S (2013) A constitutive law for rock joints considering the effects of suction and roughness on strength parameters. *Int J Rock Mech Min Sci* 60:333–344
- Zhao J (1996) Joint surface matching and shear strength part A: joint matching coefficient (JMC). *Int J Rock Mech Min Sci* 39:539–553